nature climate change

Supplementary information https://doi.org/10.1038/s41558-026-02762-2

Earlier and faster heatwave onset on land under a warming climate

In the format provided by the authors and unedited

Supplementary Information

Supplementary Note 1. Global patterns and trends in conventional heatwave metrics.

All conventional heatwave metrics except average intensity increased significantly across global land areas and in both hemispheres under the primary heatwave detection windows (Supplementary Figs. 26-30; see Methods). A 15-year centered moving-window analysis revealed marked increases in heatwave count (0.32 ± 0.01 events per decade; $p < 0.001$), heatwave days (1.52 ± 0.08 days per decade; $p < 0.001$), and the duration of the longest heatwave events (0.27 ± 0.02 days per decade; $p < 0.001$; Supplementary Fig. 26). The average intensity showed no significant trend (-0.005 ± 0.003°C per decade, $p = 0.47$), whereas cumulative heat—representing total excess heat during heatwave days—increased significantly (Supplementary Fig. 26). The spatial extent of heatwaves expanded from 52.2% of global land area in 1979 to 96.0% in 2023 (excluding Antarctica; Supplementary Fig. 18). Extending the detection windows to April-October in the Northern Hemisphere and October-April in the Southern Hemisphere yielded even stronger upward trends in heatwave frequency, duration, cumulative heat (Supplementary Fig. 29). Consistent upward trends were observed in both hemispheres (Supplementary Fig. 28), and analyses using two independent datasets (Berkeley Earth and JRA-3Q) further confirmed the robustness of the findings (Supplementary Figs. 12-14). Collectively, these results demonstrate widespread increases in heatwave frequency, duration, cumulative heat, and spatial extent over recent decades, providing important climatic context for the observed shifts in heatwave timing.

Increasing trends in heatwave frequency, duration and cumulative heat occurred across more than 92.7% of global land areas, with particularly pronounced changes between approximately 30°N and 30°S (Supplementary Fig. 27). When the analysis was stratified by long-term aridity, distinct differences in heatwave responses emerged among climate zones. Hyper-arid regions showed faster increases in frequency (0.38 ± 0.01 events per decade; $p < 0.001$) and duration (1.52 ± 0.08 days per decade; $p < 0.001$), but a smaller increase in cumulative heat (1.57 ± 0.12°C per decade; $p < 0.001$) due to a decline in annual average intensity (-0.022 ± 0.004°C per decade; $p < 0.001$; Supplementary Fig. 26). By contrast, humid regions experienced greater rises in cumulative heat (2.53±0.18°C per decade; $p < 0.001$) and affected areas (+27.4% in humid regions Vs. +4.8% in hyper-arid regions from 1979 to 2023; Supplementary Fig. 26). These contrasts reveal systematic differences in changes in heatwave characteristics among aridity zones.

Compared with 1979-2000, heatwaves during 2001-2023 were more frequent, affected more days, and generated greater cumulative heat across global land (Supplementary Fig. 26). The mean number of heatwave events increased from 1.96 ± 0.23 to 2.70 ± 0.58 events per year ($p < 0.001$), heatwave days from 8.20 ± 1.15 to 11.88 ± 3.21 days per year ($p < 0.001$), and cumulative heat from 13.43 ± 2.02 to 19.55 ± 5.64 °C per year ($p < 0.001$). Similar increases occurred across all aridity zones and most IPCC AR6 land regions (Supplementary Fig. 26 and 30). Regional patterns broadly mirrored global changes, with nearly half of the IPCC AR6 land regions exhibiting increases greater than the corresponding global average (Supplementary Fig. 30). Particularly pronounced increases occurred in parts of Central and South America, Europe, the Mediterranean, Russia, eastern Africa, Asia, and Australia.

Supplementary Note 2. Climatic context of heatwave timing shifts.

To place the observed timing shifts in a broader climatic context, we examined conventional heatwave metrics over 1979-2023. Heatwave activity intensified markedly over the past four decades, coinciding with global warming of approximately 0.15-0.20 °C per decade[64,65]. Heatwaves became more frequent and intense, lasting longer and affected larger areas (Supplementary Figs. 27-30; Supplementary Note 1), consistent with global assessments for 1950-2014[1] and the IPCC AR6 assessment[64]. The affected land area increased from 52.2% to 96.0% (Supplementary Note 1), in agreement with a recent global assessment[4]. Detrended global cumulative heat was also positively correlated with detrended global mean temperature across three independent datasets (ERA5, r = 0.62; Berkeley Earth, r = 0.58; and JRA-3Q, r = 0.66; all $p < 0.001$; Supplementary Fig. 32), indicating a close association between interannual global temperature variability and cumulative heat extremes. Together, these changes provide the climatic context for the earlier heatwave onset and longer heatwave season observed here.

Regional disparities in heatwave intensification were most evident during 2001-2023 (Supplementary Note 1). In lower mid-latitudes, such as Southern Europe and the Mediterranean region, persistent atmospheric high-pressure systems (“heat domes”) can lead to prolonged periods of extreme heat[66,67]. While the temporal changes in these systems were not quantified here, previous studies have linked such circulation patterns to severe heat extremes, particularly in parts of North America[14,68]. However, long-term trends in atmospheric blocking remain uncertain and vary by region, season, blocking metric and model framework[69]. Global analyses linking circulation anomalies and heatwave timing also remain scarce. Dryland regions showed larger increases in heatwave frequency, intensity and duration than humid regions, while heatwave onset advanced more rapidly in arid and semi-arid regions than in humid regions. This contrast may reflect stronger soil moisture-temperature feedbacks under limited water availability, which can enhance surface heating and promote earlier heatwave development[70]. Thus, atmospheric circulation and land-atmosphere coupling may shape spatial variation in heatwave timing against the broader background of intensifying heat extremes.

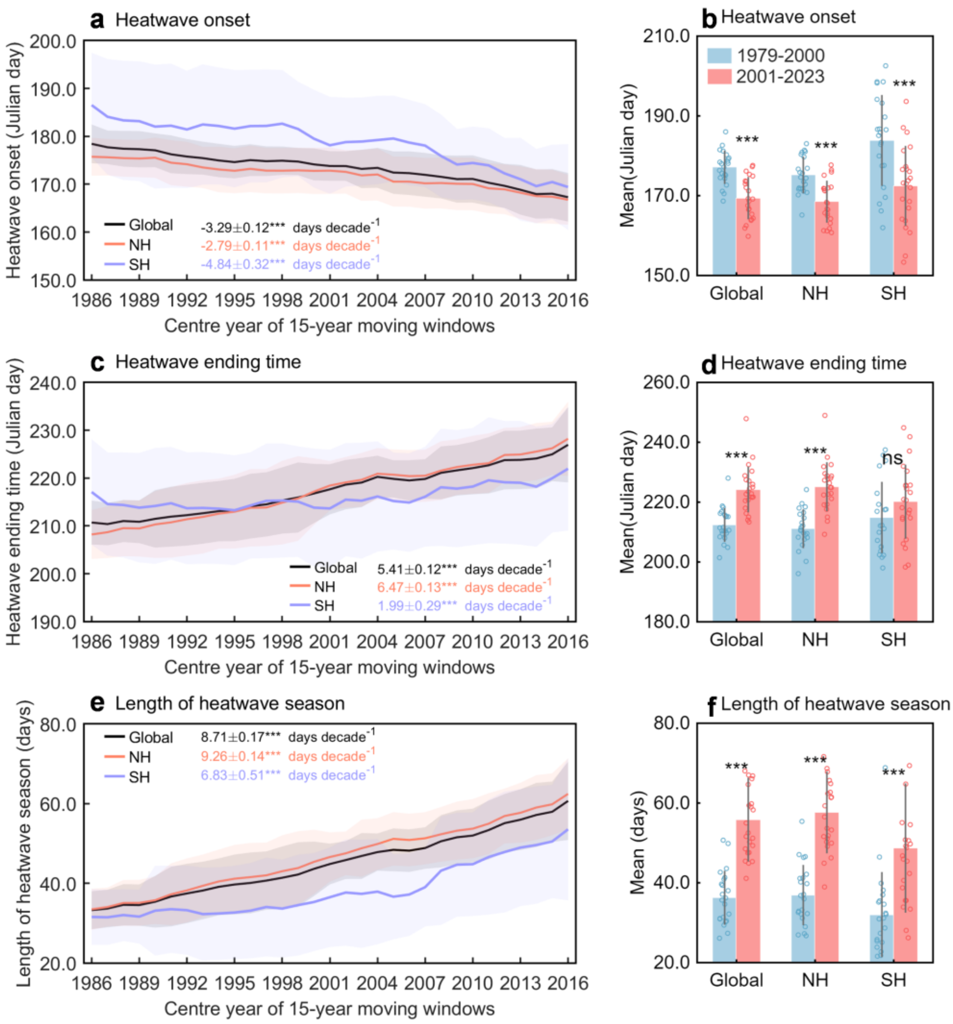

Supplementary Fig. 1 Temporal changes in heatwave onset, heatwave ending time, and length of heatwave season across hemispheres. Panels in the first column show temporal changes in heatwave onset (**a**), heatwave ending time (**c**), and length of heatwave season (**e**) globally and in the Northern Hemisphere (NH) and Southern Hemisphere (SH; excluding Antarctica), calculated using 15-year moving windows from 1979 to 2023. Heatwaves were detected using the primary detection window, defined as May-September in the Northern Hemisphere and November-March in the Southern Hemisphere. Numbers indicate linear trends (slope ± 1SE). Shaded areas indicate the corresponding standard deviation (±1 SD) of the 15-year moving-window means. The second column (**b**, **d**, and **f**) compares the corresponding metrics between 1979-2000 and 2001-2023. Individual points represent annual area-weighted means. Bars and error bars represent the period mean ±1 SD across years for global land and each aridity zone (n = 22 annual values for 1979-2000 and n = 23 annual values for 2001-2023). Trend significance was assessed using linear regression, and differences between the two periods were evaluated using two-sided, unpaired Student's t-tests. Asterisks following the trend estimates in the first column and above the bars in the second column indicate significance (***, $p < 0.001$; **, $p < 0.01$; *, $p < 0.05$); "ns" indicates $p \geq 0.05$. Exact p-values are provided in Supplementary Table 3.

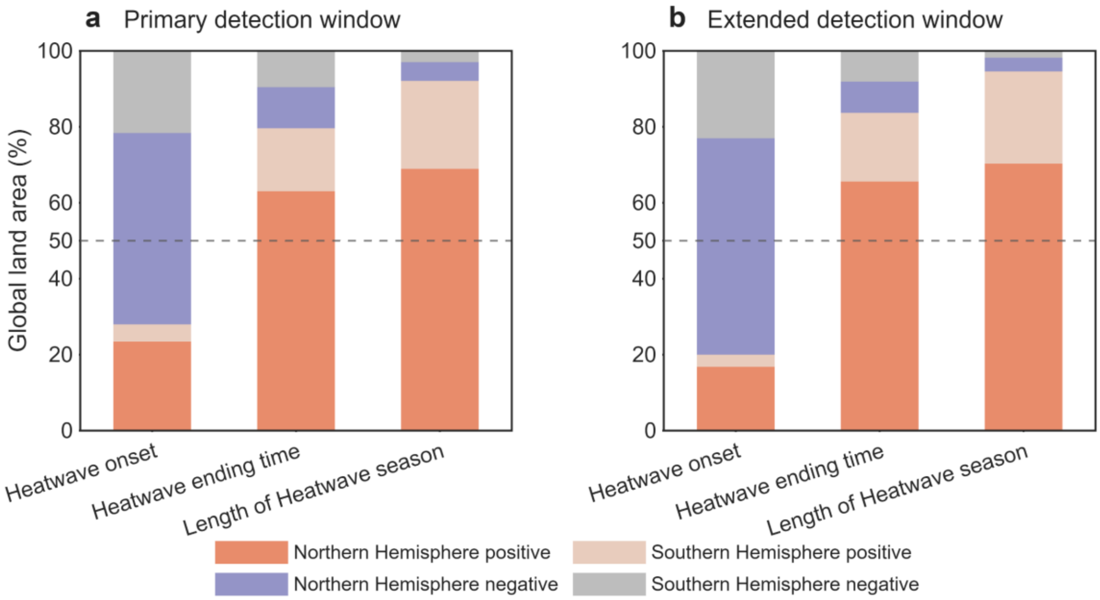

Supplementary Fig. 2 Land-area fractions of positive and negative trends in heatwave timing metrics. Fractions are shown for heatwave onset, heatwave ending time, and length of heatwave season, calculated relative to global land area excluding Antarctica, with the Northern and Southern Hemisphere components shown separately. Panel **a** shows results based on the primary detection window, defined as May-September in the Northern Hemisphere and November-March in the Southern Hemisphere. Panel **b** shows results based on the extended detection window, defined as April-October in the Northern Hemisphere and October-April in the Southern Hemisphere.

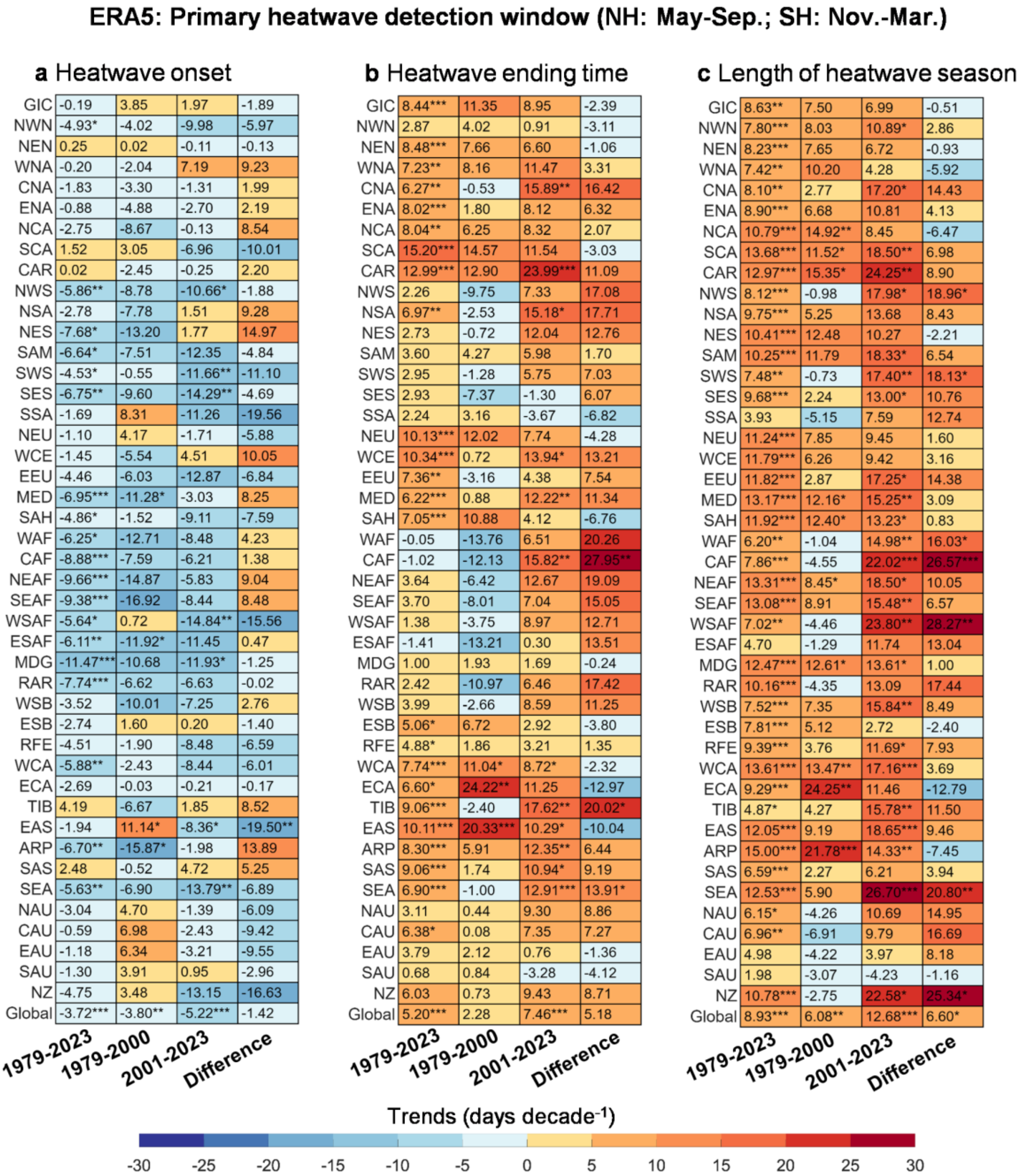

Supplementary Fig. 3 Decadal trends in heatwave timing metrics across global land regions. The figure shows changes in heatwave onset, heatwave ending time, and length of heatwave season globally and across IPCC AR6 reference regions, based on ERA5 data. Color shading shows linear trends per decade for each metric during 1979-2023 (n = 45 annual values), 1979-2000 (n = 22 annual values), and 2001-2023 (n = 23 annual values), as well as differences in mean values between the latter two periods (2001-2023 minus 1979-2000). Trend significance was assessed using linear regression, and period differences were assessed using two-sided, unpaired Student's t-tests. Asterisks denote statistical significance (***, $p < 0.001$; **, $p < 0.01$; *, $p < 0.05$). Heatwaves were detected from May to September in the Northern Hemisphere and from November to March in the Southern Hemisphere.

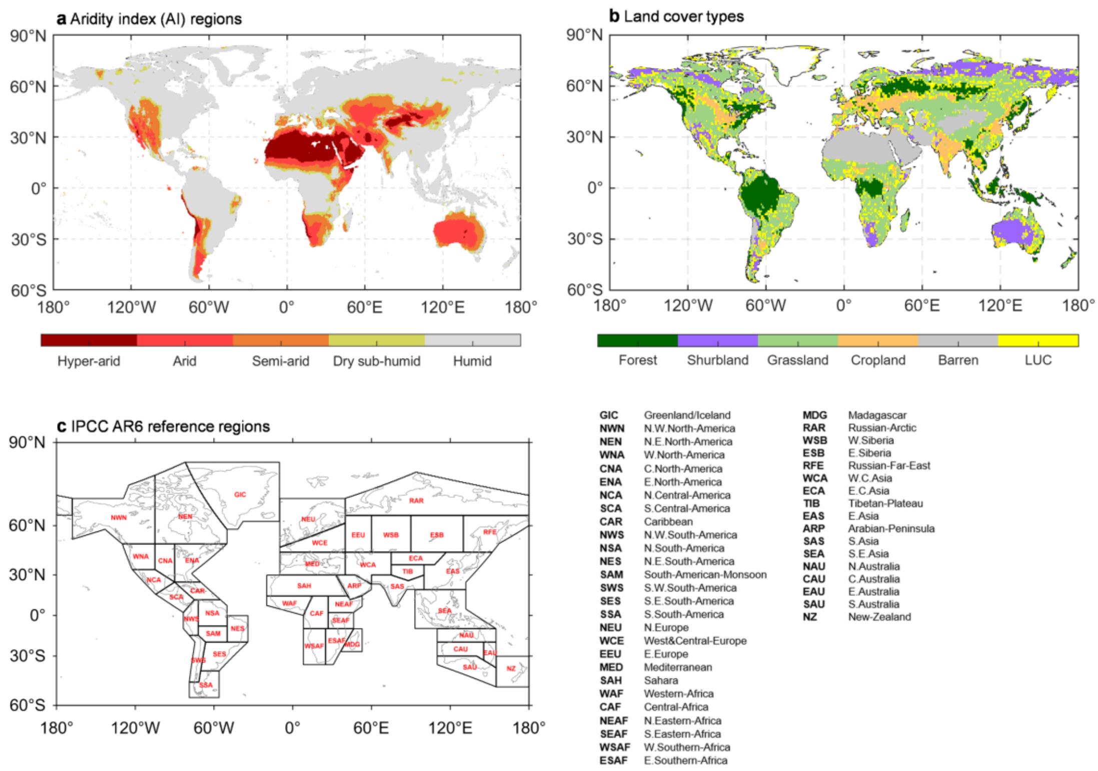

Supplementary Fig. 4 Spatial distributions of aridity regions, land-cover types, and IPCC AR6 reference regions. The aridity index (AI) classification for 1961-1990 was derived from the TerraClimate dataset (approximately 4-km spatial resolution). AI values were categorized into five classes: hyper-arid ($AI \leq 0.05$), arid ($0.05 < AI \leq 0.20$), semi-arid ($0.20 < AI \leq 0.50$), dry sub-humid ($0.50 < AI \leq 0.65$), and humid ($AI > 0.65$). Land-cover types were classified as forest, shrubland, grassland, cropland, and barren land based on grid cells with unchanged MODIS land cover (MCD12C1) between 2001 and 2023. The IPCC AR6 reference regions are shown for the regional assessments. Basemaps are from Natural Earth (www.naturalearthdata.com).

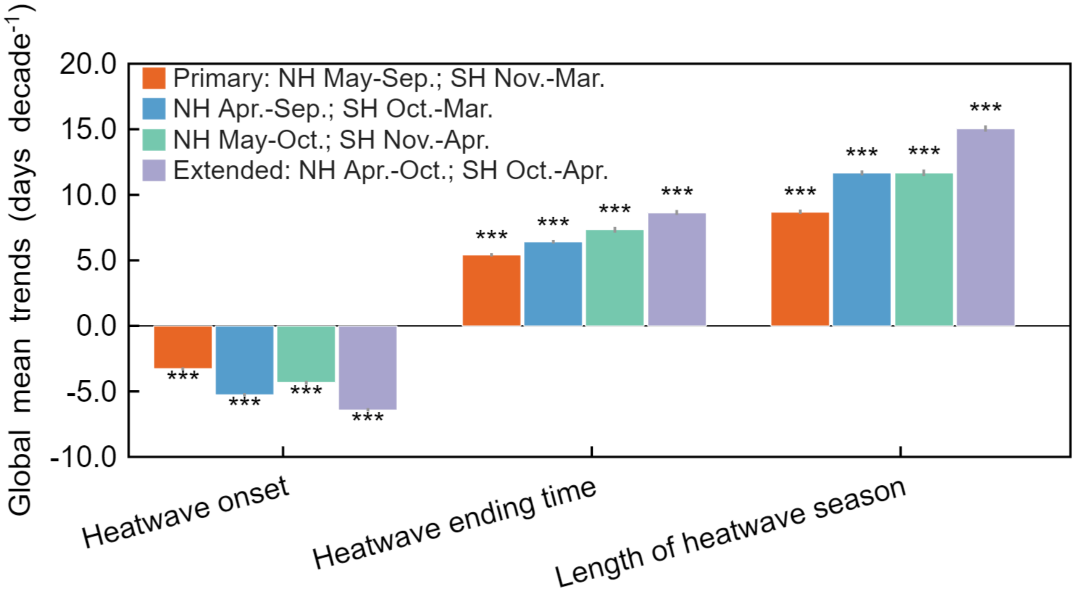

Supplementary Fig. 5 Sensitivity of global heatwave timing trends to alternative detection windows, based on ERA5 data for 1979-2023. Bars show global mean trends (days per decade) in heatwave onset, heatwave ending time, and length of heatwave season, derived from 15-year moving averages of annual area-weighted global means. Results are shown for four detection-window definitions named according to their Northern Hemisphere warm season: May-September, April-September, May-October and April-October. The corresponding Southern Hemisphere windows were November-March, October-March, November-April, and October-April, respectively. Error bars indicate the standard errors of the estimated linear trends, and asterisks denote trend significance (***, $p < 0.001$; **, $p < 0.01$; *, $p < 0.05$). Trends were assessed using linear regression based on the 15-year moving-window series (n = 31 moving-window values).

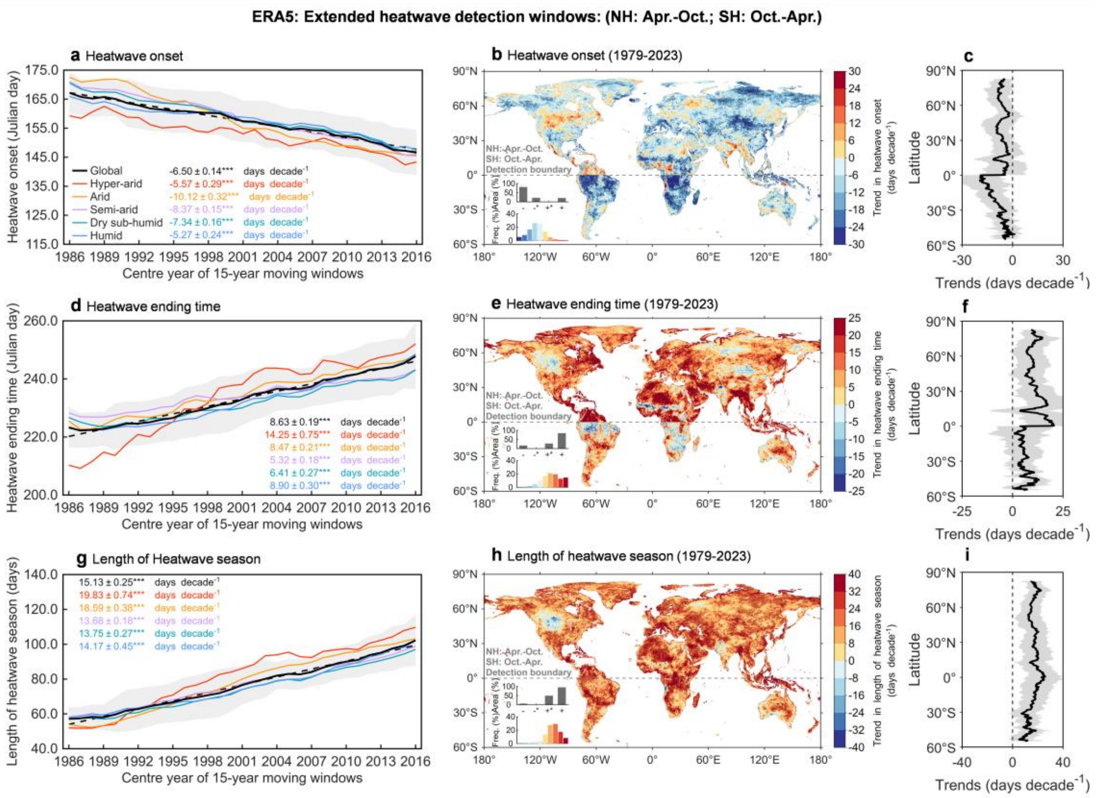

Supplementary Fig. 6 Temporal and spatial trends in heatwave timing metrics using extended heatwave detection windows. Heatwave onset, heatwave ending time, and length of heatwave season during 1979-2023 were analyzed using ERA5 hourly data. Panels **a**, **d**, and **g** show 15-year centred moving averages of annual area-weighted means globally and across aridity zones. In each panel, the black solid line denotes the global moving average, grey shading indicates ±1 SD of the annual area-weighted means within each 15-year window, and the black dashed line shows the fitted linear trend. Colored solid lines denote the moving averages for different aridity zones (i.e., hyper-arid, arid, semi-arid, dry sub-humid, and humid), and numbers in the corresponding colors indicate the slope ± 1 SE of the fitted linear trend, with asterisks denoting statistical significance (***, $p < 0.001$; **, $p < 0.01$; *, $p < 0.05$). Temporal trends were assessed by linear regression using the moving-window series (n = 31 values). Panels **b**, **e**, and **h** show spatial trends per decade across land grid cells (excluding Antarctica), assessed by linear regression using annual values (n = 45 years). Plus signs indicate statistically significant trends ($p < 0.05$). Statistical significance was assessed at the native 0.25° resolution, whereas plus signs are displayed at 1° intervals for visual clarity. The upper inset bar charts show the fractions of global land area with non-significant negative (−), significant negative (−*), significant positive (+*), and non-significant positive (+) trends, respectively. The lower inset histograms show the frequency distributions of grid-cell trends. The dashed horizontal line marks the Equator. Heatwaves were detected using April-October in the Northern Hemisphere and October-April in the Southern Hemisphere as the extended detection windows. Panels **c**, **f**, and **i** show the corresponding latitudinal distributions of each timing metric. Basemaps are from Natural Earth (www.naturalearthdata.com).

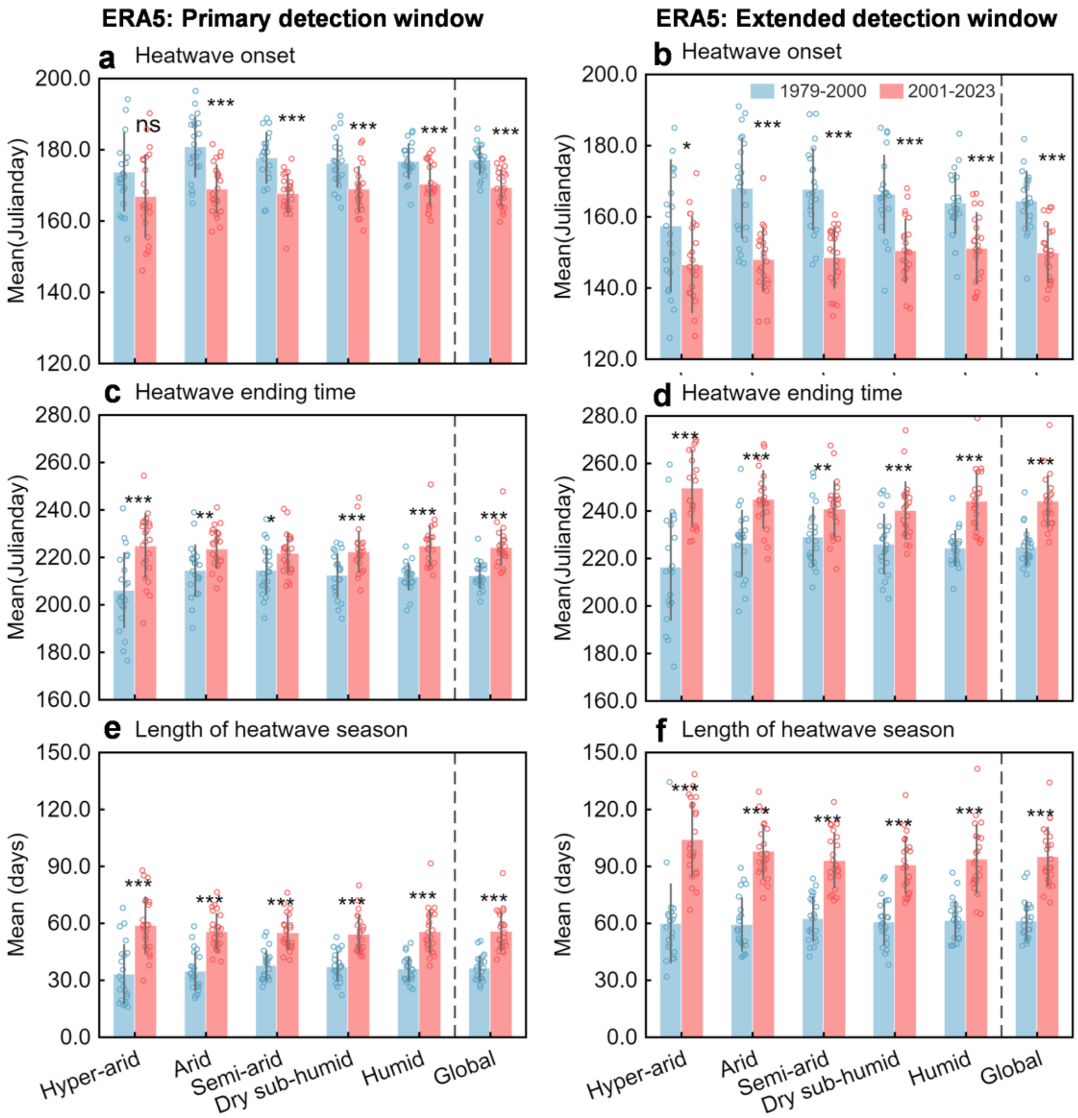

Supplementary Fig. 7 Period differences in heatwave timing under primary and extended detection windows. Heatwave onset, ending time and length of heatwave season are compared between 1979-2000 and 2001-2023 using ERA5 hourly data. The left and right columns show results based on the primary and extended detection windows, respectively. The primary heatwave detection window covered May-September in the Northern Hemisphere and November-March in the Southern Hemisphere; the extended window covered April-October and October-April, respectively. Individual points represent annual area-weighted means. Bars and error bars represent the period mean ±1 SD across years for global land and each aridity zone (n = 22 annual values for 1979-2000 and n = 23 annual values for 2001-2023). Asterisks above the bars and "ns" indicate statistically significant (***, p<0.001; **, $p < 0.01$; *, $p < 0.05$) and non-significant differences between the two periods, respectively. Differences between the two periods were evaluated using two-sided, unpaired Student's t-tests. Exact p-values for period comparisons are provided in Supplementary Table 3.

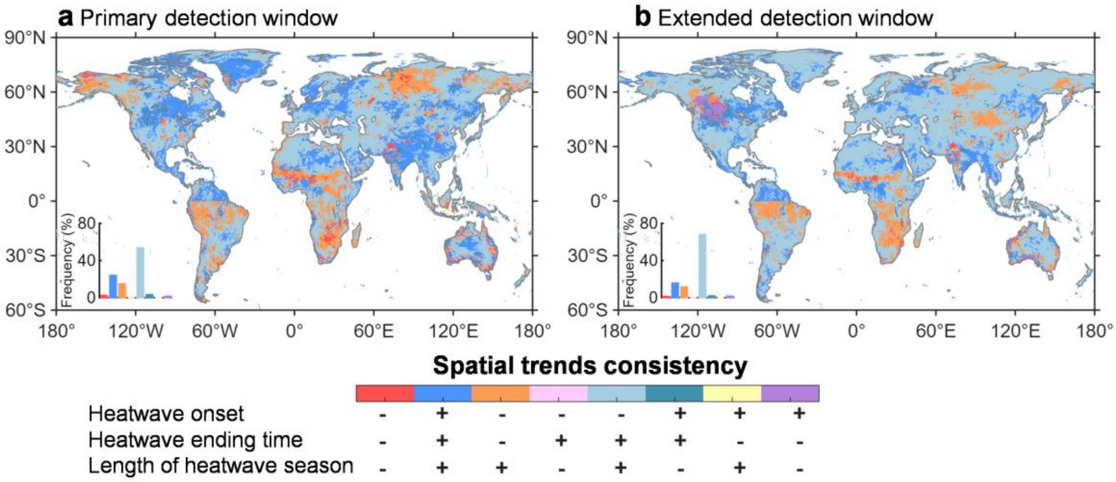

Supplementary Fig. 8 Spatial consistency among heatwave timing trends under primary and extended detection windows. Panels **a** and **b** show the spatial distributions of the eight possible combinations of positive and negative trends in heatwave onset, ending time and length of heatwave season during 1979-2023 under the primary and extended detection windows, respectively. The inset bar charts show the percentages of land grid cells corresponding to each trend-direction combination. The primary heatwave detection window covered May-September in the Northern Hemisphere and November-March in the Southern Hemisphere; the extended window covered April-October and October-April, respectively. Basemaps are from Natural Earth (www.naturalearthdata.com).

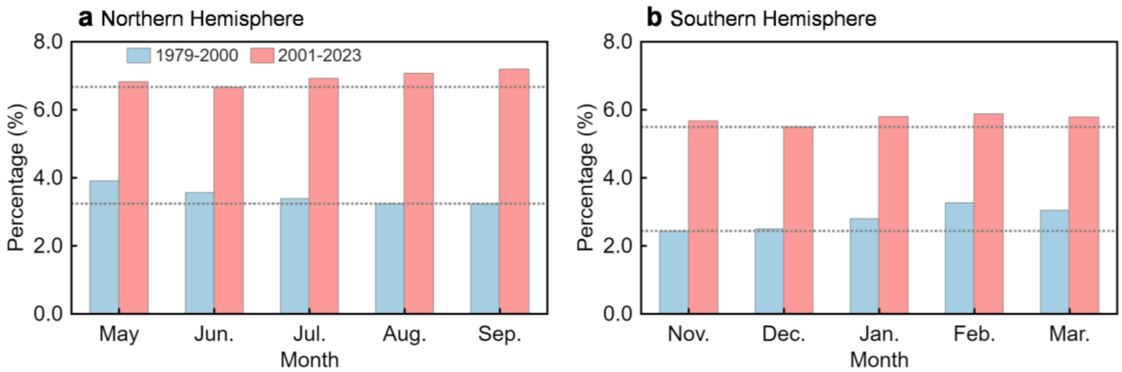

Supplementary Fig. 9 Seasonal distribution of heatwave days between 1979-2000 and 2001-2023 under the primary heatwave detection window. Heatwaves were detected during May-September in the Northern Hemisphere (**a**) and November-March in the Southern Hemisphere (**b**)**.** Bar plots show the percentage of land grid-days experiencing heatwaves in each month, calculated by aggregating daily (Julian-day-based) heatwave occurrences across all years within each period and normalizing by the total number of land grid-days within the corresponding detection window for each hemisphere. Blue and red bars represent the periods of 1979-2000 and 2001-2023, respectively. Dotted horizontal lines indicate the minimum monthly percentage within each period.

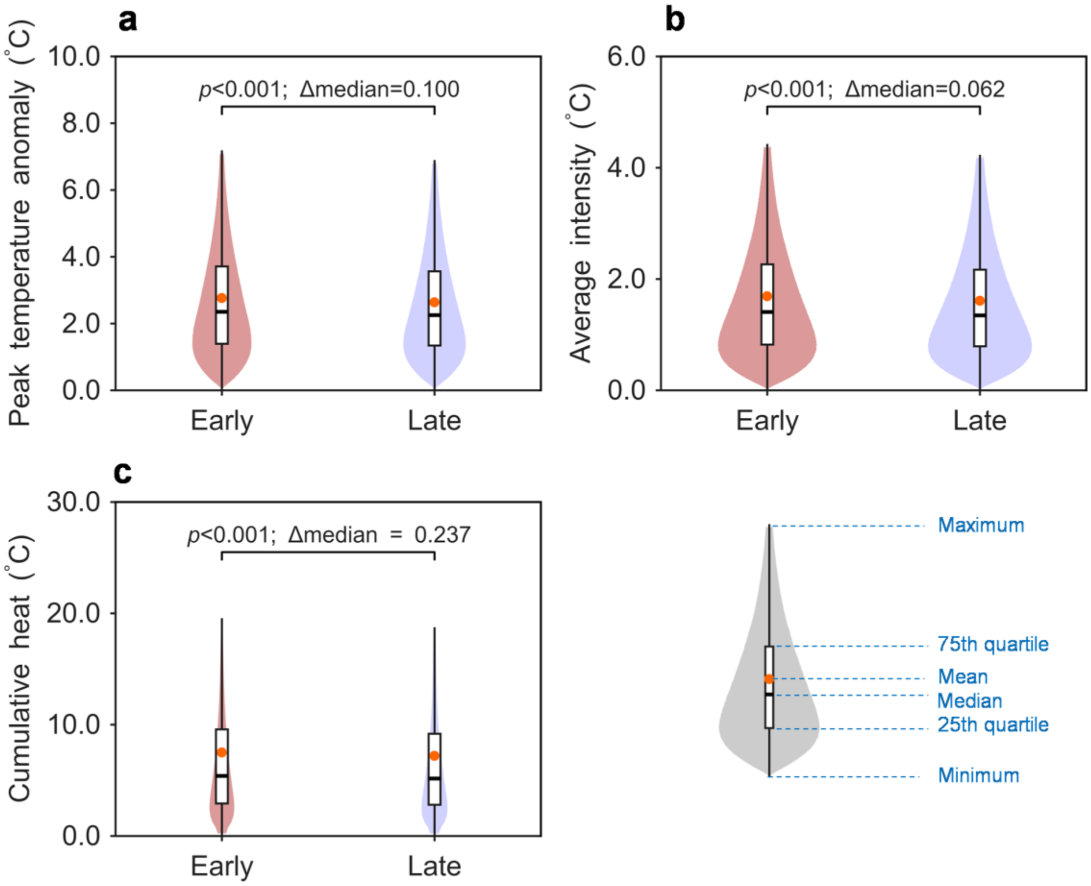

Supplementary Fig. 10 Differences in heatwave characteristics between early- and late-season heatwaves. Early- and late-season heatwaves were defined as the first and last heatwaves detected in each year, respectively, across global land grid cells during 1979-2023. Heatwaves were identified using the primary heatwave detection window, defined as May-September in the Northern Hemisphere and November-March in the Southern Hemisphere. Panels **a-c** show the distributions of peak temperature anomaly, average intensity, and cumulative heat. Boxes denote the interquartile ranges, black horizontal lines indicate the medians, red dots indicate the means, and whiskers indicate the minimum and maximum values. Differences between early- and late-season heatwaves were assessed using two-sided Mann-Whitney U tests. Figure annotations show the corresponding *p* values and Δmedian (Δmedian=median$_{early}$–median$_{late}$).

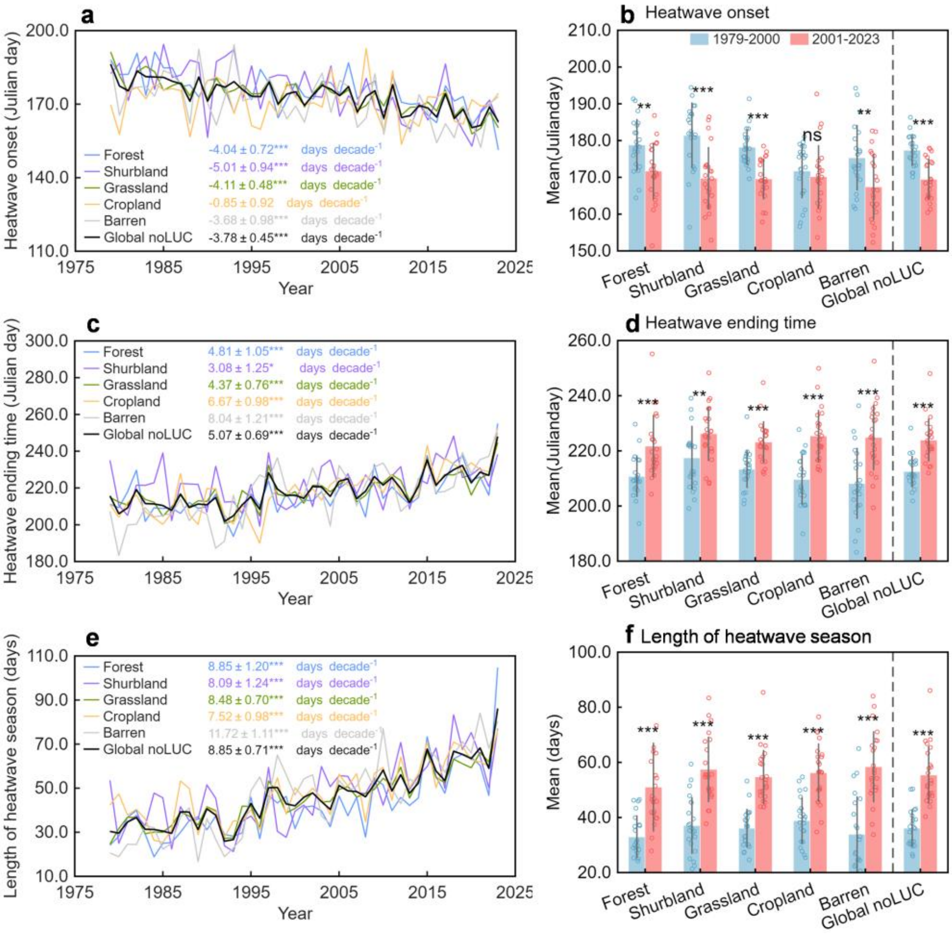

Supplementary Fig. 11 Temporal changes in heatwave timing across stable land-cover types. Heatwaves were detected using the primary detection window, defined as May-September in the Northern Hemisphere and November-March in the Southern Hemisphere. Panels **a**, **c**, and **e** show annual area-weighted means and linear trends in heatwave onset, heatwave ending time, and length of heatwave season, respectively, for forest, shrubland, grassland, cropland, and barren land. Land-cover types were identified from grid cells whose MODIS land-cover classes (MCD12C1) remained unchanged during 2001-2023. Global averages across all grid cells with no land-use change (noLUC) are also shown for comparison. Colored numbers indicate the linear trend slopes ± 1 SE, with asterisks denoting statistical significance. Linear trends were assessed using linear regression based on the annual series from 1979 to 2023 (n = 45 annual values). Panels **b**, **d**, and **f** compare the corresponding mean values of each heatwave metric between 1979-2000 and 2001-2023. Individual points represent annual area-weighted means. For each land-cover type and for global noLUC, bars and error bars represent the period mean ±1 SD (n = 22 annual values for 1979-2000 and n = 23 annual values for 2001-2023). Differences between periods were assessed using two-sided, unpaired Student's t-tests. Asterisks above the bars and "ns" indicate statistically significant (***, $p < 0.001$; **, $p < 0.01$; *, $p < 0.05$) and non-significant differences between the two periods, respectively. Exact p-values for both linear trends and period comparisons are provided in Supplementary Table 3.

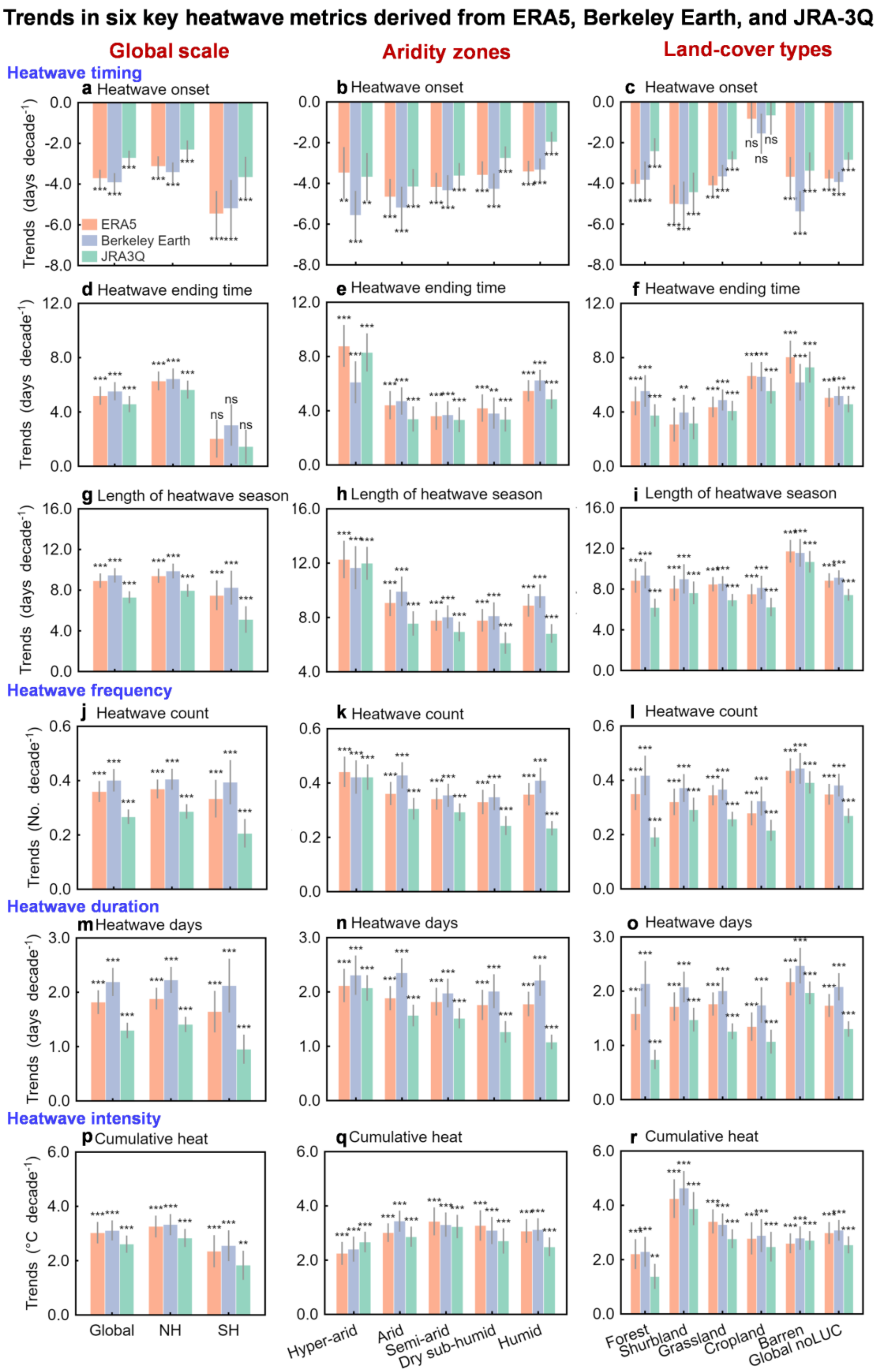

Supplementary Fig. 12 Trends in six key heatwave metrics across the ERA5, Berkeley Earth, and JRA-3Q datasets under the primary heatwave detection window. Heatwaves were detected during May-September in the Northern Hemisphere and November-March in the Southern Hemisphere. The panels show trends (per decade) in various heatwave metrics, including heatwave timing (i.e., heatwave onset, heatwave ending time, and length of heatwave season), heatwave frequency (heatwave count), heatwave duration (heatwave days), and heatwave intensity (cumulative heat). Columns show results at the global scale (left), across aridity zones (middle; hyper-arid, arid, semi-arid, dry sub-humid, and humid), and across land-cover types (right; forest, shrubland, grassland, cropland, barren land, and global noLUC areas). Orange, purple, and green bars represent ERA5, Berkeley Earth, and JRA-3Q, respectively. Bars and error bars indicate slopes ±1 SE of the corresponding linear trend estimates for 1979-2023. Asterisks above the bars and “ns” indicate statistically significant (***, $p < 0.001$; **, $p < 0.01$; *, $p < 0.05$) and non-significant trends, respectively.

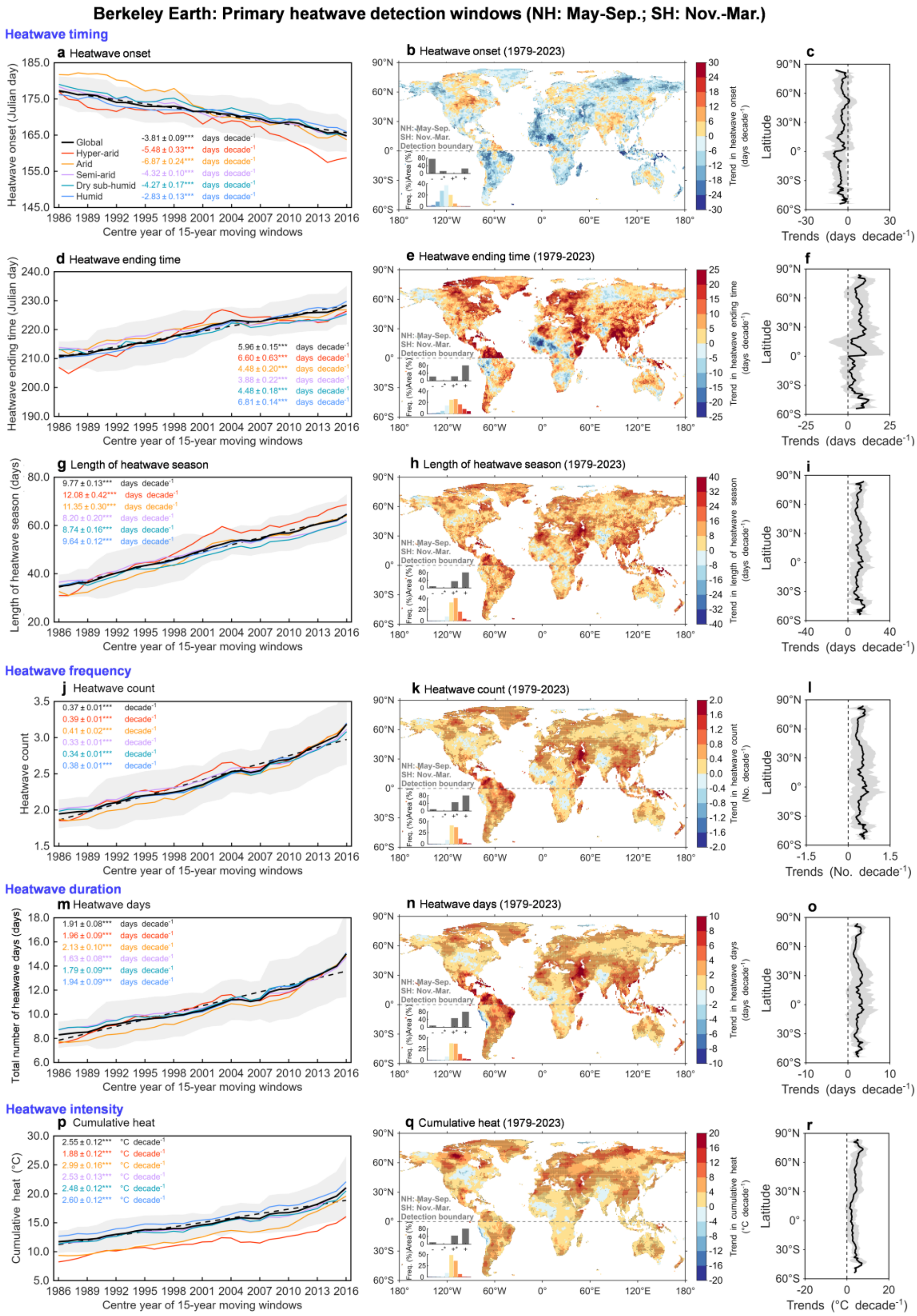

Supplementary Fig. 13 Temporal and spatial trends in six key heatwave metrics during 1979-2023 under the primary heatwave detection window, based on the Berkeley Earth dataset. Rows show heatwave onset (row 1), heatwave ending time (row 2), length of heatwave season (row 3), heatwave frequency (heatwave count; row 4), heatwave duration (heatwave days; row 5), and heatwave intensity (cumulative heat;

row 6). Panels in the first column show global temporal changes based on 15-year centered moving averages of annual area-weighted global means across land grid cells. The grey shading indicates the interannual (temporal) standard deviation of the 15-year moving-window means, and the black dashed lines show the fitted linear trends. Colored numbers indicate the slope ± 1 SE of the fitted linear trend for the corresponding series, with asterisks denoting statistical significance (***, $p < 0.001$; **, $p < 0.01$; *, $p < 0.05$). Temporal trends were assessed using linear regression based on the moving-window series (n = 31 values). Panels in the second column show spatial trends per decade in the corresponding heatwave metrics during the same period across land grid cells (excluding Antarctica). Spatial trends were assessed using linear regression based on annual values (n = 45 years). Grid cells with statistically significant trends ($p < 0.05$) are marked with "+". The dashed horizontal line marks the Equator. Heatwaves were detected using the primary detection window, defined as May-September in the Northern Hemisphere and November-March in the Southern Hemisphere. Panels in the third column show the corresponding latitudinal distributions. Basemaps are from Natural Earth (www.naturalearthdata.com).

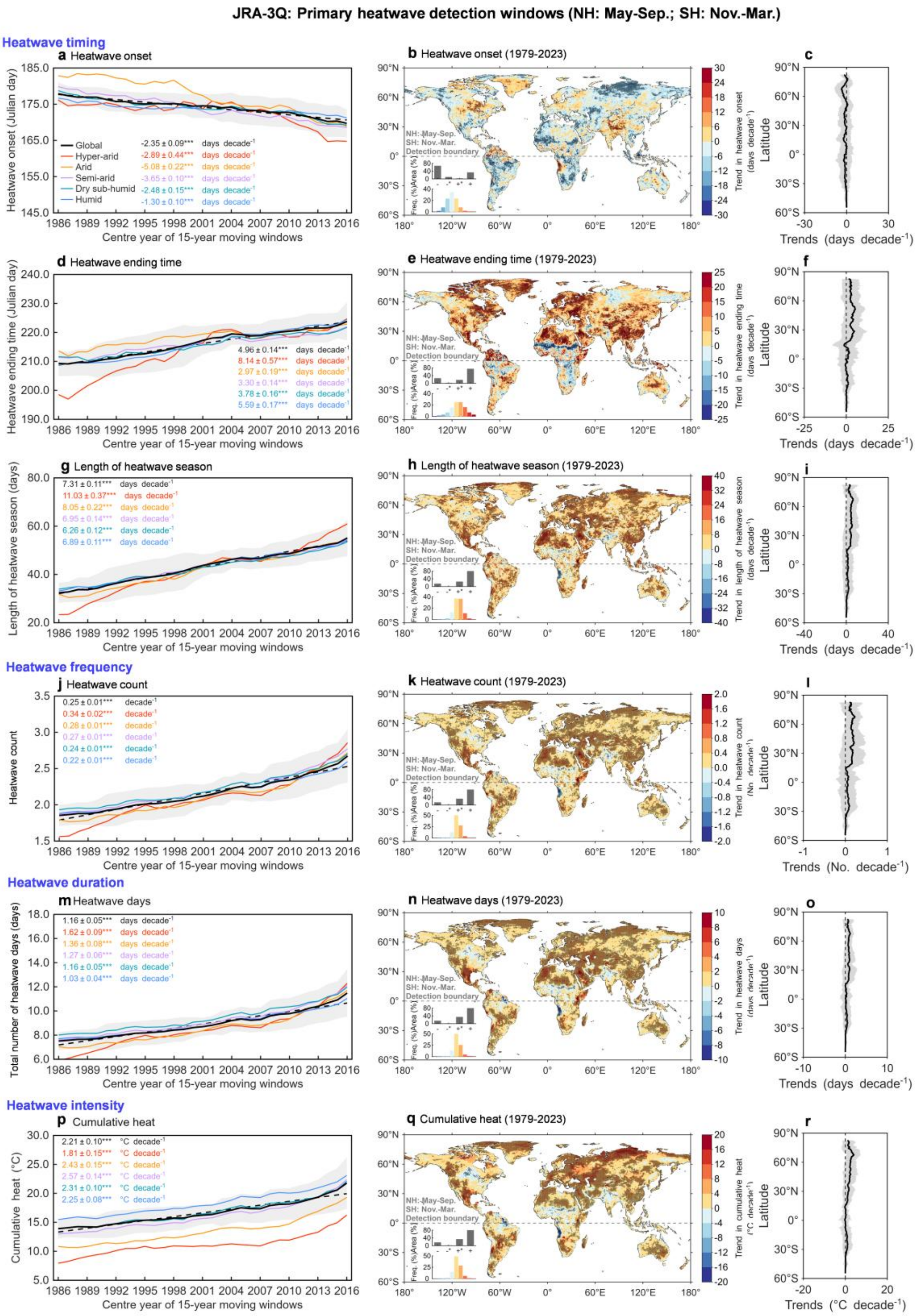

Supplementary Fig. 14 Temporal and spatial trends in six key heatwave metrics during 1979-2023 under the primary heatwave detection window, based on the JRA-3Q dataset. Rows show heatwave onset (row 1), heatwave ending time (row 2), length of heatwave season (row 3), heatwave frequency (heatwave count; row 4), heatwave duration (heatwave days; row 5), and heatwave intensity (cumulative heat;

row 6). Panels in the first column show global temporal changes based on 15-year centered moving averages of annual area-weighted global means across land grid cells. The grey shading indicates the interannual (temporal) standard deviation of the 15-year moving-window means, and the black dashed lines show the fitted linear trends. Colored numbers indicate the slope ± standard error of the fitted linear trend for the corresponding series, with asterisks denoting statistical significance (***, $p < 0.001$; **, $p < 0.01$; *, $p < 0.05$). Temporal trends were assessed using linear regression based on the moving-window series ($n = 31$ values). Panels in the second column show spatial trends per decade in the corresponding heatwave metrics during the same period across land grid cells (excluding Antarctica). Spatial trends were assessed using linear regression based on annual values ($n = 45$ years). Grid cells with statistically significant trends ($p < 0.05$) are marked with "+". The dashed horizontal line marks the Equator. Heatwaves were detected using the primary detection window, defined as May-September in the Northern Hemisphere and November-March in the Southern Hemisphere. Panels in the third column show the corresponding latitudinal distributions. Basemaps are from Natural Earth (www.naturalearthdata.com).

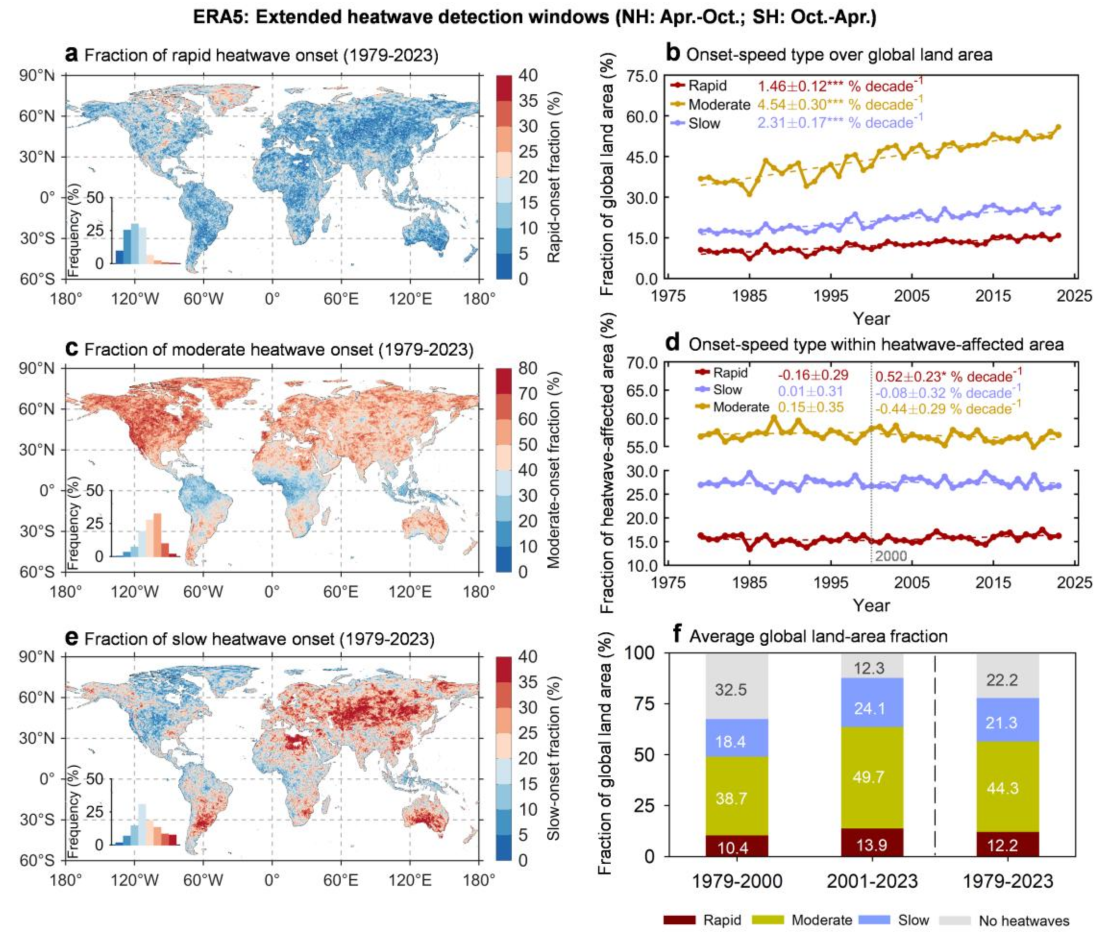

Supplementary Fig. 15 Spatial and temporal patterns of the rapid, moderate, and slow onset-speed types of the first heatwaves during 1979-2023 under the extended heatwave detection window, based on ERA5 data. Heatwaves were detected during April-October in the Northern Hemisphere and October-April in the Southern Hemisphere. **a**, Spatial distribution of the observed fraction of first heatwaves classified as the rapid onset-speed type during 1979-2023. **c**, Same as **a**, but for the moderate onset-speed type. **e**, Same as **a**, but for the slow onset-speed type. **b**, Time series of the fraction of global land area for which the first heatwave was classified as the rapid, moderate, or slow onset-speed type. **d**, Time series of the fraction of heatwave-affected land area classified as each onset-speed type. The dashed vertical line marks the year 2000, separating the two subperiods. Values to the left and right of the line indicate the linear regression slopes ± 1SE based on annual values for 1979-2000 (n=22) and 2001-2023 (n=23), respectively. Asterisks in **b** and **d** indicate the statistical significance of the fitted temporal trends (***, $p < 0.001$; **, $p < 0.01$; *, $p < 0.05$). **f**, Mean global land-area fractions for each onset-speed type over three periods (1979-2000, 2001-2023, and 1979-2023). A vertical line separates the summaries for the two subperiods (left) from the full-period summary (right). Basemaps are from Natural Earth (www.naturalearthdata.com).

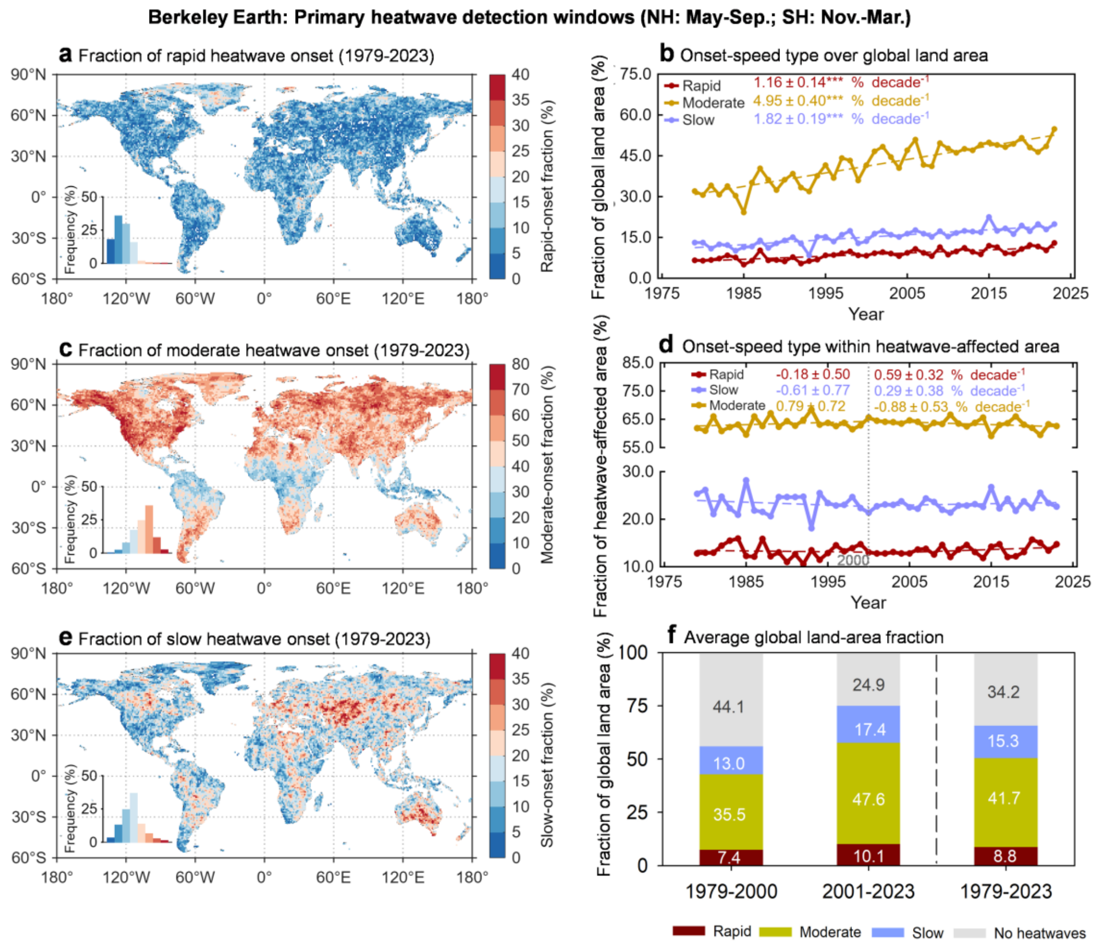

Supplementary Fig. 16 Spatial and temporal patterns of the rapid, moderate, and slow onset-speed types of the first heatwaves during 1979-2023 under the primary heatwave detection window, based on Berkeley Earth data. Heatwaves were detected during May-September in the Northern Hemisphere and November-March in the Southern Hemisphere. **a,** Spatial distribution of the observed fraction of first heatwaves classified as the rapid onset-speed type during 1979-2023. **c**, Same as **a**, but for the moderate onset-speed type. **e**, Same as **a**, but for the slow onset-speed type. **b**, Time series of the fraction of global land area for which the first heatwave was classified as the rapid, moderate, or slow onset-speed type. **d**, Time series of the fraction of heatwave-affected land area classified as each onset-speed type. The dashed vertical line marks the year 2000, separating the two subperiods. Values to the left and right of the line indicate the linear regression slopes ± 1SE based on annual values for 1979-2000 (n=22) and 2001-2023 (n=23), respectively. Asterisks in b and d indicate the statistical significance of the fitted temporal trends (***, $p < 0.001$; **, $p < 0.01$; *, $p < 0.05$). **f**, Mean global land-area fractions for each onset-speed type over three periods (1979-2000, 2001-2023, and 1979-2023). A vertical line separates the summaries for the two subperiods (left) from the full-period summary (right). Basemaps are from Natural Earth (www.naturalearthdata.com).

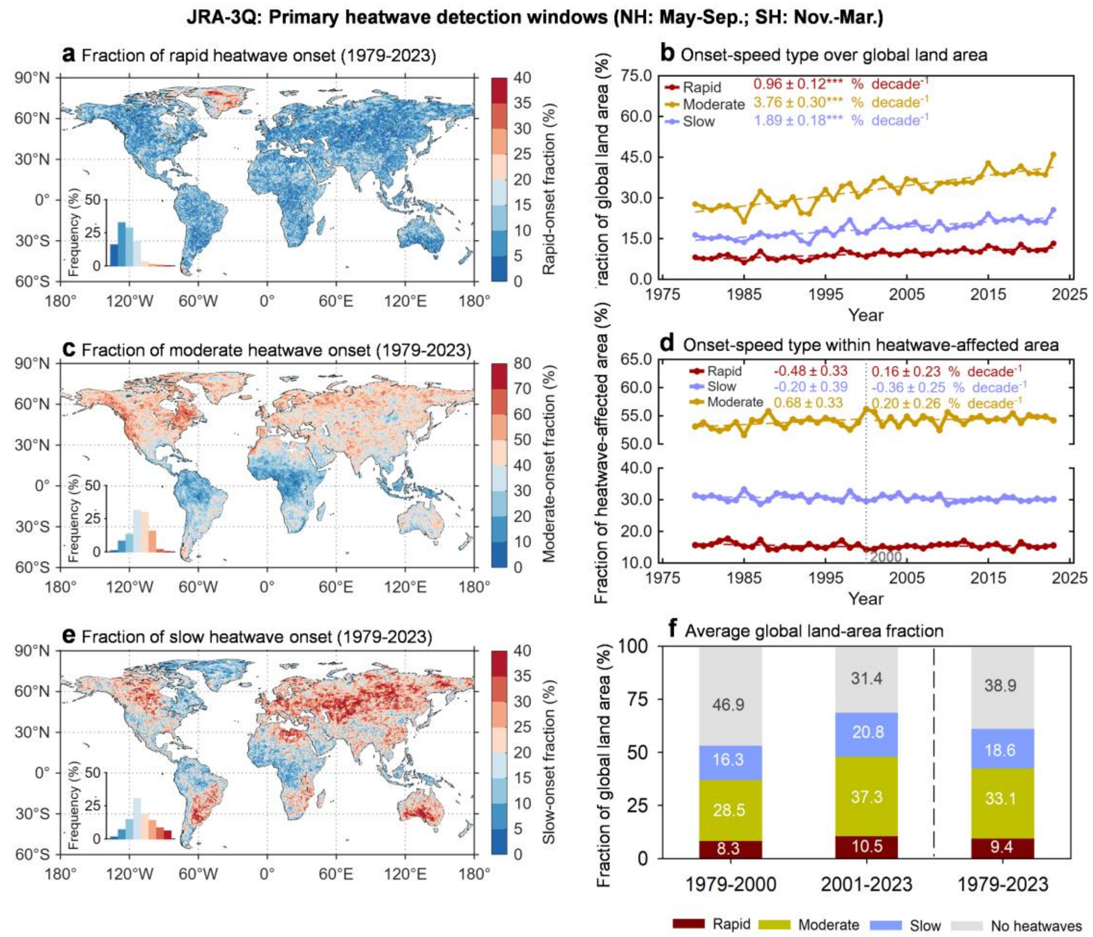

Supplementary Fig. 17 Spatial and temporal patterns of the rapid, moderate, and slow onset-speed types of the first heatwaves during 1979-2023 under the primary heatwave detection window, based on JRA-3Q data. Heatwaves were detected during May-September in the Northern Hemisphere and November-March in the Southern Hemisphere. **a**, Spatial distribution of the observed fraction of first heatwaves classified as the rapid onset-speed type during 1979-2023. **c**, Same as **a**, but for the moderate onset-speed type. **e**, Same as **a**, but for the slow onset-speed type. **b**, Time series of the fraction of global land area for which the first heatwave was classified as the rapid, moderate, or slow onset-speed type. **d**, Time series of the fraction of heatwave-affected land area classified as each onset-speed type. The dashed vertical line marks the year 2000, separating the two subperiods. Values to the left and right of the line indicate the linear regression slopes ± 1SE based on annual values for 1979-2000 (n=22) and 2001-2023 (n=23), respectively. Asterisks in **b** and **d** indicate the statistical significance of the fitted temporal trends (***, $p < 0.001$; **, $p < 0.01$; *, $p < 0.05$). **f**, Mean global land-area fractions for each onset-speed type over three periods (1979-2000, 2001-2023, and 1979-2023). A vertical line separates the summaries for the two subperiods (left) from the full-period summary (right). Basemaps are from Natural Earth (www.naturalearthdata.com).

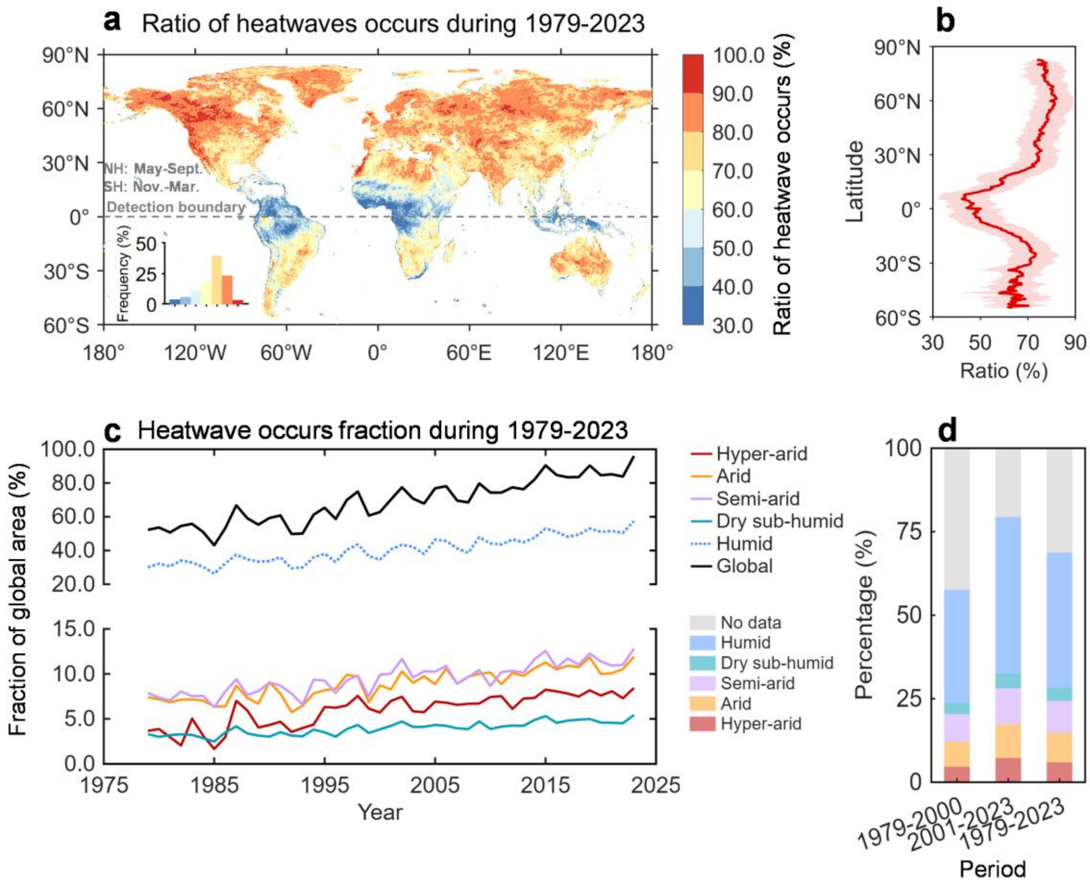

Supplementary Fig. 18 Heatwave occurrence ratio during 1979-2023, based on ERA5 data. Heatwaves were detected using the primary heatwave detection window, defined as May-September in the Northern Hemisphere and November-March in the Southern Hemisphere**. a,** Spatial pattern of the heatwave occurrence ratio during 1979-2023. The inset panel in a shows the frequency distribution across different ratio ranges. **b**, Latitudinal variation in the heatwave occurrence ratio (mean ± SD). **c**, Changes in the fraction of land experiencing heatwaves across different aridity index (AI) classes during1979-2023. AI values were classified into five categories: hyper-arid (AI ≤ 0.05), arid (0.05 < AI ≤ 0.20), semi-arid (0.20 < AI ≤ 0.50), dry sub-humid (0.50 < AI ≤ 0.65), and humid (AI > 0.65). **d**, Mean global percentage distributions across AI zones during the two subperiods (1979-2000 and 2001-2023) and over the full period (1979-2023). Basemaps are from Natural Earth (www.naturalearthdata.com).

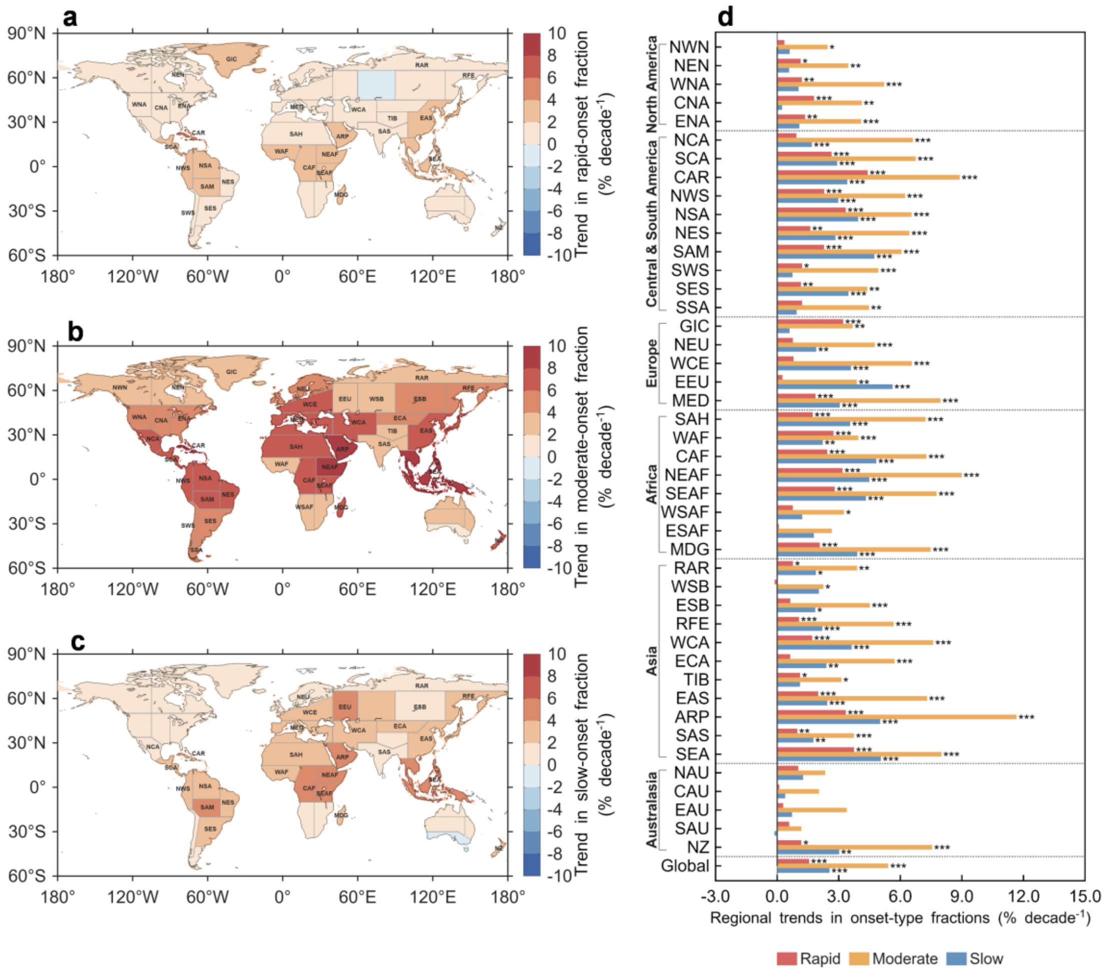

Supplementary Fig. 19 Regional trends in the fractions of land area classified by first heatwave onset-speed type across IPCC AR6 reference regions during 1979-2023. a-c, Spatial distribution of regional linear trends in the fraction of each region's total land area where the first heatwave was classified as the rapid, moderate, and slow onset-speed type, respectively, based on ERA5 data. Colors indicate trend magnitudes in percentage points per decade. Regions showing statistically significant trends (p < 0.05) are labelled with their regional abbreviations. **d**, Corresponding regional trends for the 44 IPCC AR6 reference land regions and the global land area, shown separately for the rapid, moderate, and slow onset-speed types. Regions are grouped into North America, Central and South America, Europe, Africa, Asia, and Australasia. Red, orange, and blue bars represent rapid, moderate, and slow onset-speed types, respectively. Trends were assessed using linear regression based on annual values (n = 45). Asterisks indicate the statistical significance of the linear trends (***, p < 0.001; **, p < 0.01; *, p < 0.05). Heatwaves were detected using the primary heatwave detection window, defined as May-September in the Northern Hemisphere and November-March in the Southern Hemisphere. Basemap data are from Natural Earth (www.naturalearthdata.com).

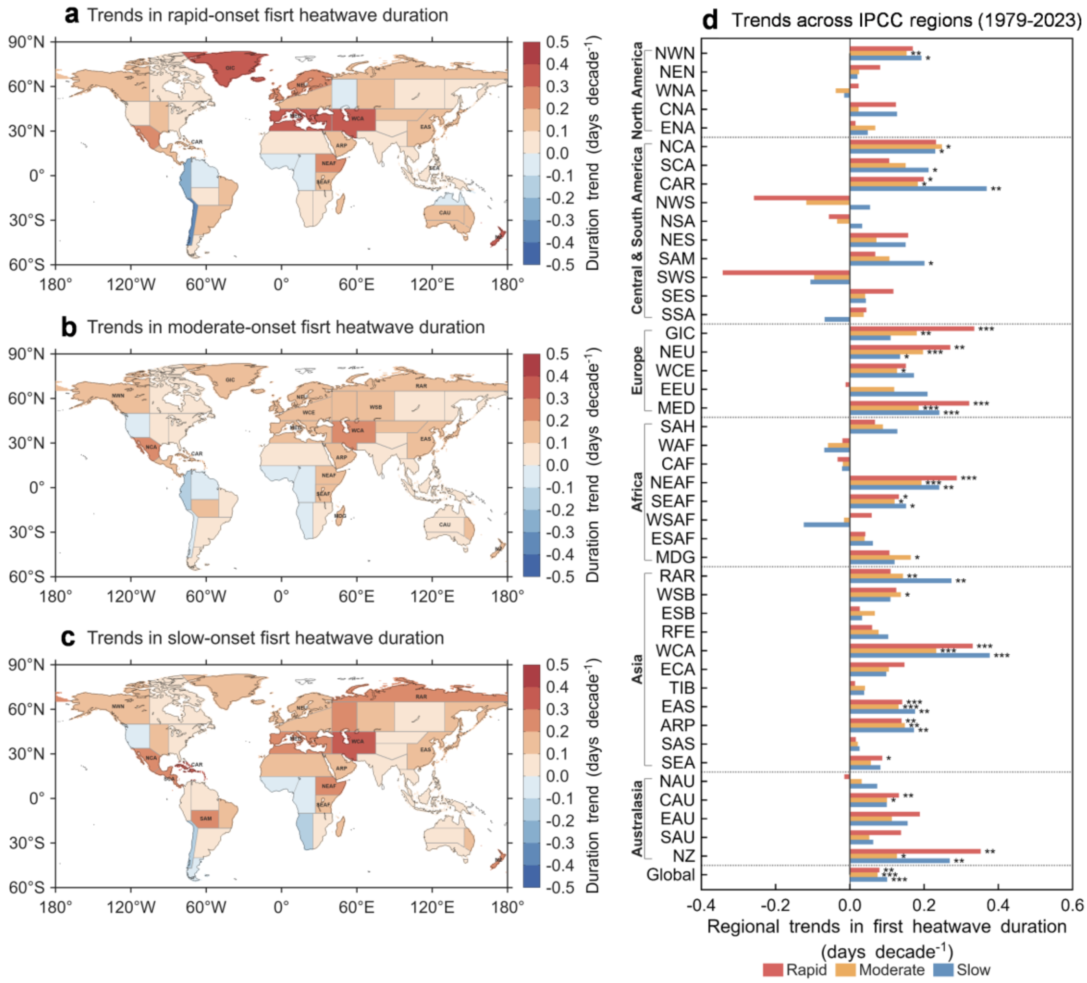

Supplementary Fig. 20 Regional trends in first heatwave duration by onset-speed type across IPCC AR6 reference regions during 1979-2023. a-c, Spatial distributions of regional linear trends in first heatwave duration for the rapid, moderate, and slow onset-speed types, respectively, based on ERA5 data. Colors indicate trend magnitudes in days per decade. For each region and onset-speed type, annual values were calculated as the land-area-weighted mean duration of the first heatwave across grid cells classified as that type. Regions with statistically significant trends ($p < 0.05$) are labelled with their regional abbreviations. **d**, Corresponding trends in regional land-area-weighted mean duration of the first heatwave for the 44 IPCC AR6 reference land regions and the global land area, shown separately for the rapid, moderate, and slow onset-speed types. Regions are grouped into North America, Central and South America, Europe, Africa, Asia, and Australasia. Red, orange, and blue bars represent the rapid, moderate, and slow onset-speed types, respectively. Asterisks indicate the statistical significance of the linear trends (***, $p < 0.001$; **, $p < 0.01$; *, $p < 0.05$). Heatwaves were detected using the primary heatwave detection window, defined as May-September in the Northern Hemisphere and November-March in the Southern Hemisphere. Basemaps are from Natural Earth (www.naturalearthdata.com).

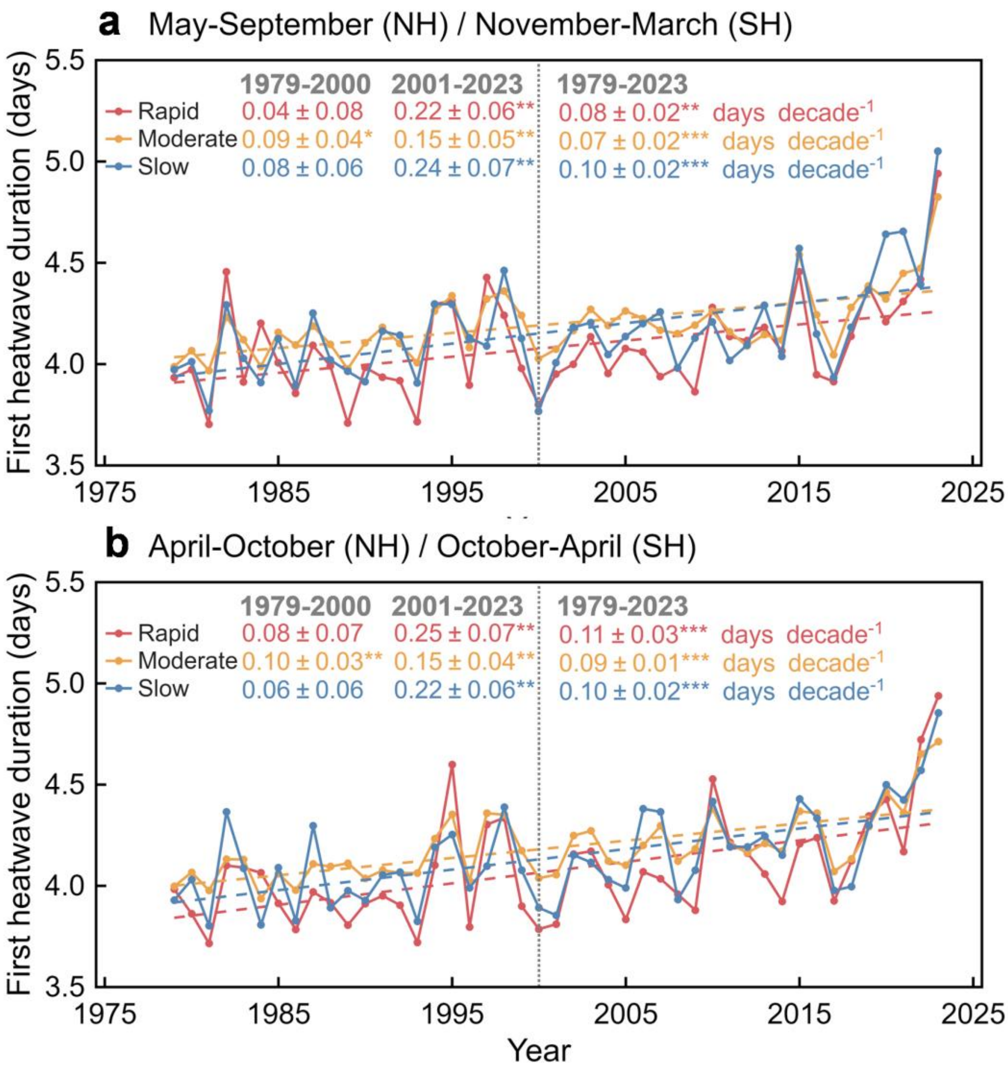

Supplementary Fig. 21 Global temporal changes in first heatwave duration by onset-speed type under the primary and extended heatwave detection windows from 1979 to 2023. a, Global land-area-weighted mean durations of rapid-, moderate-, and slow-onset first heatwaves under the primary detection window, defined as May-September in the Northern Hemisphere and November-March in the Southern Hemisphere. **b**, Same as **a**, but under the extended detection window, defined as April-October in the Northern Hemisphere and October-April in the Southern Hemisphere. Colored solid lines with circles show annual values, and the vertical dotted line marks the year 2000, separating the two subperiods. Dashed lines in the corresponding colors show the fitted linear trends for the full period (1979-2023). Colored values indicate linear-regression slopes ± 1 SE for the two subperiods (1979-2000 and 2001-2023) and the full period (1979-2023), expressed in days per decade. Asterisks indicate statistically significant trends (***, $p < 0.001$; **, $p < 0.01$; *, $p < 0.05$).

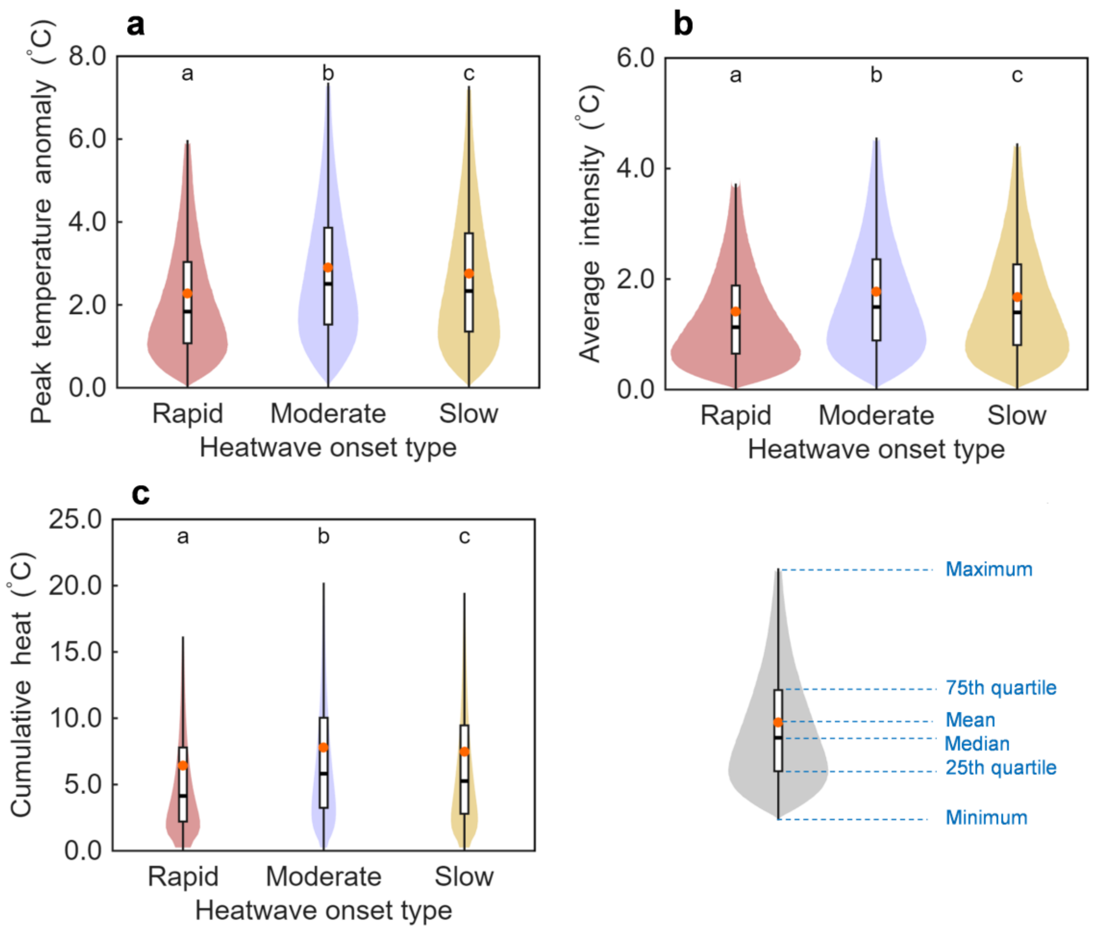

Supplementary Fig. 22 Differences in first heatwave characteristics among onset-speed types classified by the relative timing of peak temperature within each event. Heatwaves were categorized into rapid, moderate, and slow onset-speed types based on whether the temperature peak occurred in the first, middle, or final third of the heatwave duration, respectively. Violin plots show distributions of (**a**) peak temperature anomaly, (**b**) average intensity, and (**c**) cumulative heat for the first heatwave event within the primary heatwave detection window, defined as May-September in the Northern Hemisphere and November-March in the Southern Hemisphere during 1979-2023. Boxes represent interquartile ranges, black horizontal lines indicate medians, and red dots show means. Different letters above the groups denote statistically significant pairwise differences between onset-speed types (Kruskal-Wallis test with post hoc multiple comparisons, $p < 0.05$).

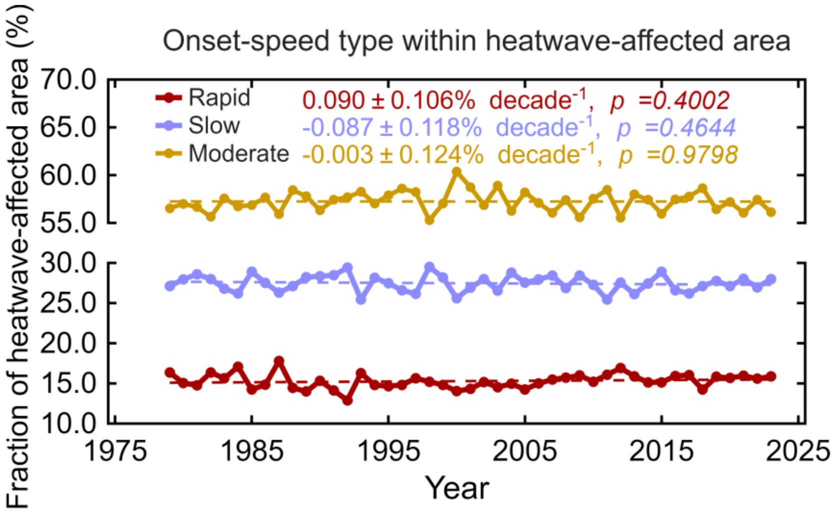

Supplementary Fig. 23 Time series of the fraction of heatwave-affected land area classified into the rapid, moderate, and slow onset-speed types during 1979-2023, based on ERA5 data. Heatwaves were detected using the primary heatwave detection window, defined as May-September in the Northern Hemisphere and November-March in the Southern Hemisphere. Colored solid lines with circles show annual values for the rapid, moderate, and slow onset-speed types. Dashed lines in the corresponding colors show the fitted linear trends over the full study period (1979-2023). Colored values indicate the linear trend slopes ± standard errors, expressed in percentage points per decade. Trend significance was assessed using linear regression (n = 45 annual values).

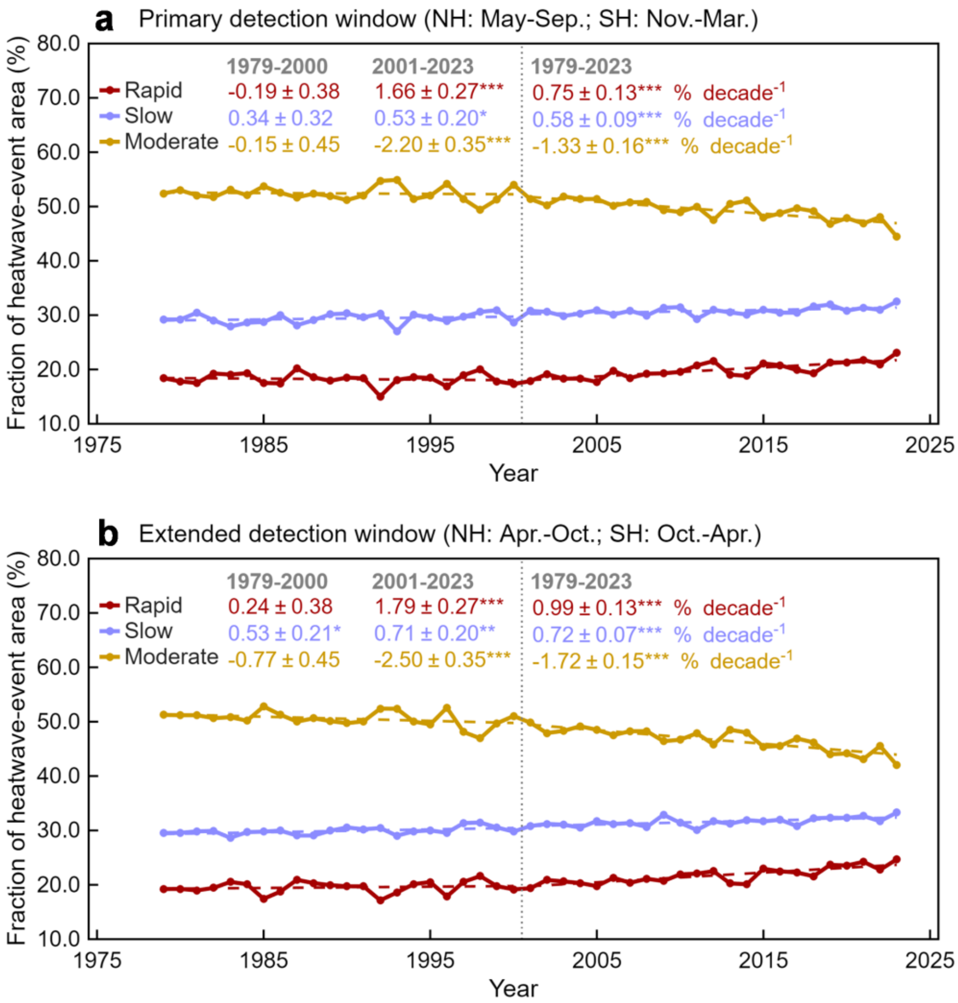

Supplementary Fig. 24 Temporal changes in heatwave-affected area fractions by onset-speed type. Fractions of the total heatwave-affected area associated with rapid-, moderate-, and slow-onset events are shown for all heatwave events under the primary (**a**) and extended (**b**) detection windows during 1979-2023. The primary window was defined as May-September in the Northern Hemisphere and November-March in the Southern Hemisphere, whereas the extended window was defined as April-October and October-April, respectively. The vertical dotted line indicates the year 2000 and separates the two subperiods. Colored numbers indicate linear-trend slopes ± 1 SE for 1979-2000 (n = 22 annual values), 2001-2023 (n = 23 annual values) and 1979-2023 (n = 45 annual values). Asterisks denote the statistical significance of the linear-regression slopes based on two-sided tests (***, $p < 0.001$; **, $p < 0.01$; *, $p < 0.05$).

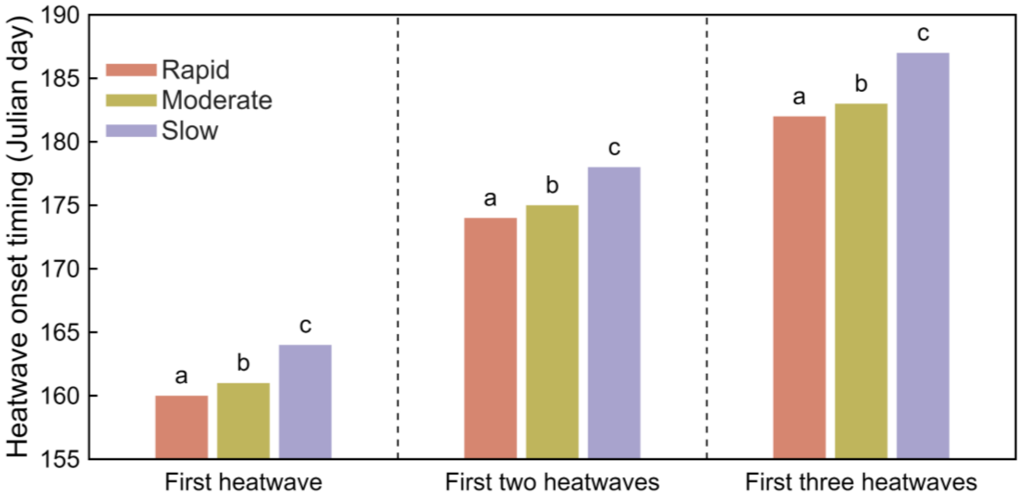

Supplementary Fig. 25 Median onset timing based on the first, first two, and first three heatwaves during 1979-2023 across global land grid cells, grouped by onset-speed type under the primary heatwave detection window. The primary window was defined as May-September in the Northern Hemisphere and November-March in the Southern Hemisphere. For each category, medians were calculated from all grid-cell events over the full study period. Letters denote statistically significant differences in medians among onset-speed types (Kruskal-Wallis tests, $p < 0.05$).

ERA5 Heatwave detection windows: (NH: May-Sep.; SH: Nov.-Mar.)

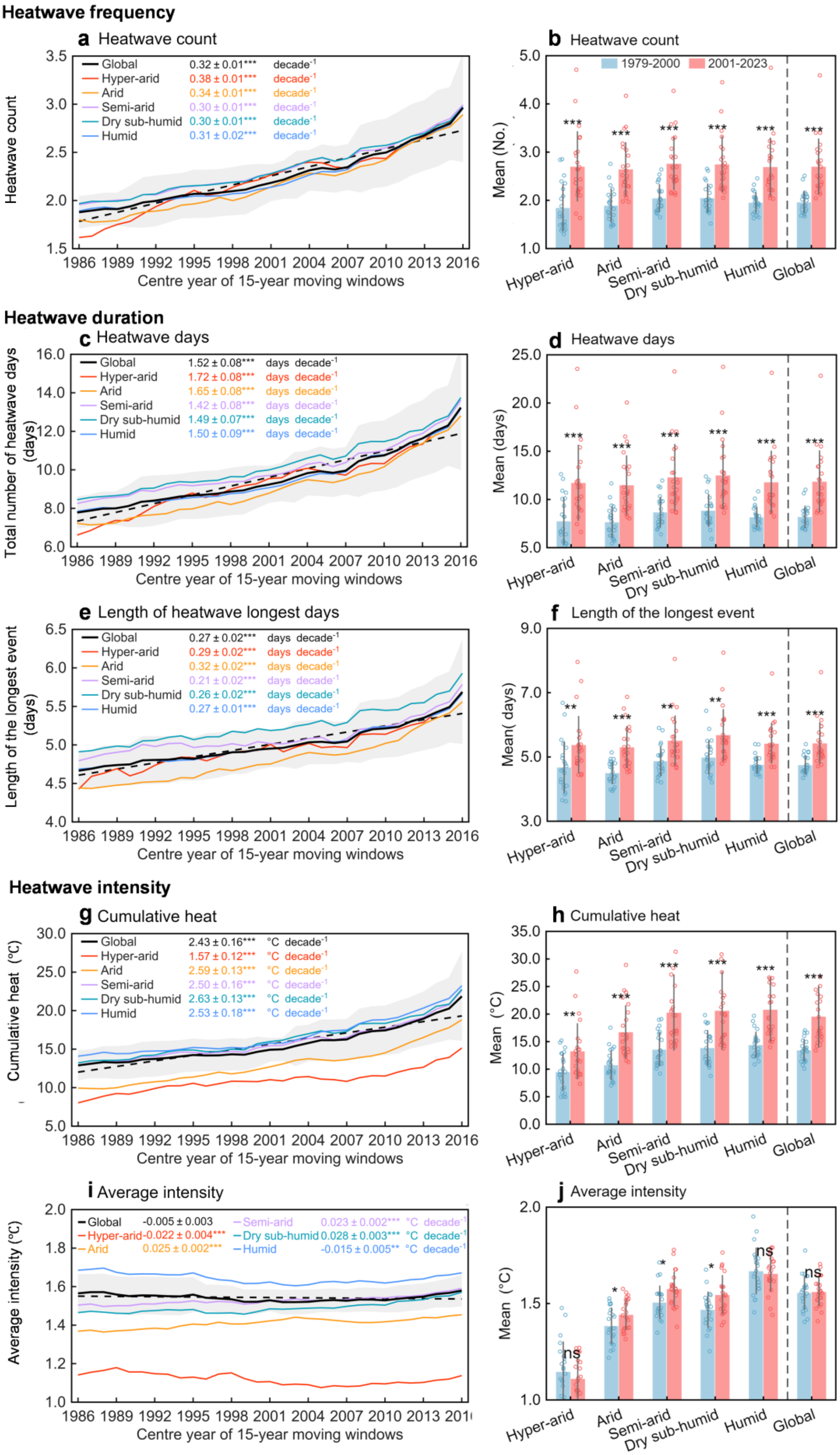

Supplementary Fig. 26 Temporal changes in heatwave frequency, duration, and intensity from 1979 to 2023 under the primary heatwave detection window. The primary heatwave detection window was defined as May-September in the Northern Hemisphere and November-March in the Southern Hemisphere. Panels **a**, **c**, **e**, **g**, and **i** show 15-year centred moving averages of annual area-weighted means for global land and the five aridity zones. In each panel, the black solid line denotes the global moving average, grey shading indicates ±1 SD of the annual area-weighted means within each 15-year window, and the black dashed line shows the fitted linear trend. Colored solid lines represent the moving averages for different aridity zones (i.e., hyper-arid, arid, semi-arid, dry sub-humid, and humid). Numbers in the corresponding colors indicate the linear trend slopes ±1 SE, with asterisks denoting statistical significance (***, $p < 0.001$; **, $p < 0.01$; *, $p < 0.05$). Linear trends were assessed using linear regression based on the 15-year centred moving-window series (n = 31 moving-window values). Panels **b**, **d**, **f**, **h**, and **j** compare the mean values of each heatwave metric between 1979-2000 (n=22 years) and 2001-2023 (n=23 years). Individual points represent annual area-weighted means, and bars and error bars indicate the period mean ±1 SD. Asterisks and "ns" above the bars indicate statistically significant and non-significant differences between the two periods, respectively. Differences between periods were assessed using two-tailed, unpaired Student's *t*-tests. *p*-values for linear trends are reported in Supplementary Table 1, and exact *p*-values for period comparisons are provided in Supplementary Table 3.

ERA5: Primary detection windows (NH: May-Sep.; SH: Nov.-Mar.)

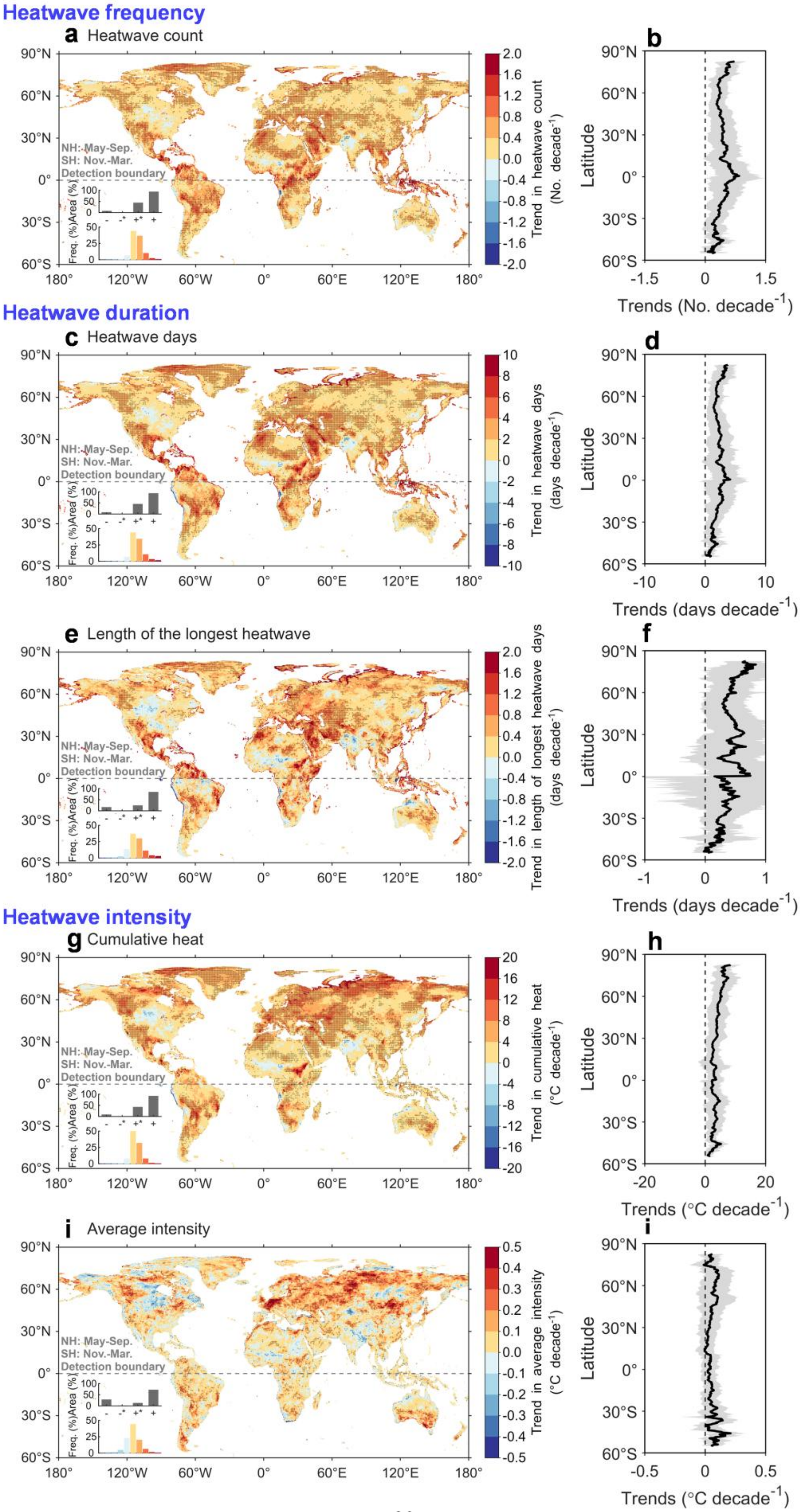

Supplementary Fig. 27 Spatial trends and latitudinal distributions of conventional heatwave metrics during 1979-2023 under the primary heatwave detection window. The primary window was defined as May-September in the Northern Hemisphere and November-March in the Southern Hemisphere. The first column shows spatial trends in heatwave frequency (**a**), heatwave days (**c**), length of longest heatwave (**e**), cumulative heat (**g**), and average intensity (**i**) across global land areas (excluding Antarctica) during 1979-2023. The second column shows latitudinal distributions of the corresponding heatwave metrics (**b**, **d**, **f**, **h**, and **j**). Spatial trends were assessed using linear regression based on annual values (n = 45 years). Plus signs indicate statistically significant trends ($p < 0.05$). Statistical significance was assessed at the native 0.25° resolution, whereas plus signs are displayed at 1° intervals for visual clarity. Basemaps are from Natural Earth (www.naturalearthdata.com).

ERA5: Primary heatwave detection windows (NH: May-Sep.; SH: Nov.-Mar.)

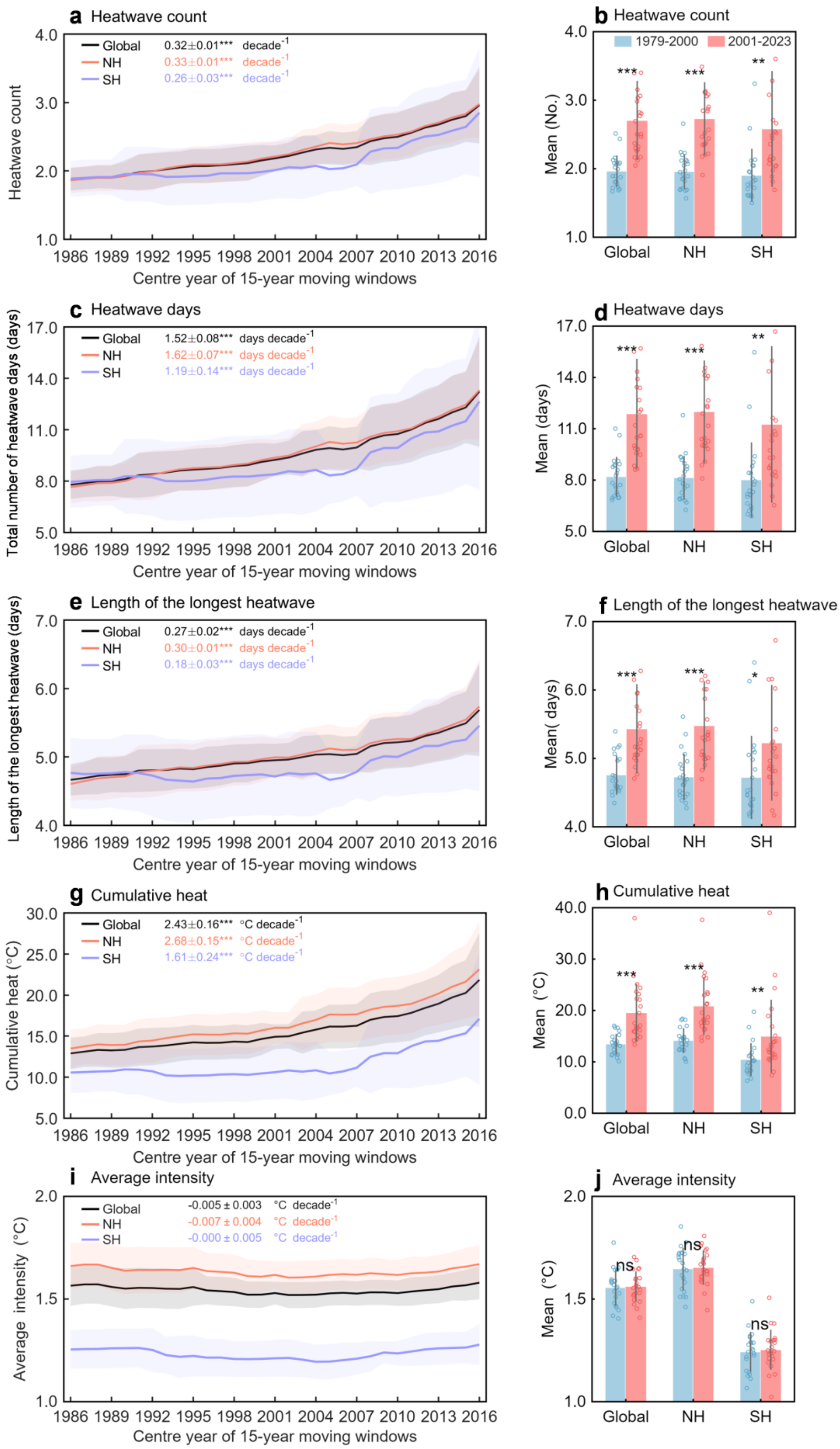

Supplementary Fig. 28 Temporal changes in heatwave frequency, duration, and intensity globally and across the Northern and Southern Hemispheres. Heatwaves were detected using the primary heatwave detection window, defined as May-September in the Northern Hemisphere and November-March in the Southern Hemisphere. Panels in the first column show temporal changes in heatwave count (**a**), heatwave days (**c**), length of the longest heatwave (**e**), cumulative heat (**g**), and average intensity (**i**) globally and for the Northern Hemisphere (NH) and Southern Hemisphere (SH; excluding Antarctica), based on a 15-year moving window from 1979 to 2023. Shaded areas in the corresponding colors indicate ±1 SD of the annual area-weighted means within each 15-year window. Colored numbers show the linear trend slopes ± 1 SE for the corresponding global, NH, and SH series, with asterisks denoting statistical significance (***, $p < 0.001$; **, $p < 0.01$; *, $p < 0.05$). Panels in the second column (**b**, **d**, **f**, **h**, and **j**) compare the corresponding metrics between 1979-2000 (n = 22 years) and 2001-2023 (n = 23 years). Individual points represent annual area-weighted means, and bars and error bars indicate the period mean ±1 SD. Linear trends were assessed using linear regression, and differences between periods were evaluated using two-sided, unpaired Student's t-tests. Asterisks above the bars and "ns" indicate statistically significant (***, $p < 0.001$; **, $p < 0.01$; *, $p < 0.05$) and non-significant differences between the two periods, respectively. Exact p-values for both linear trends and period comparisons are provided in Supplementary Table 3.

ERA5: Extended heatwave detection windows (NH: Apr.-Oct.; SH: Oct.-Apr.)

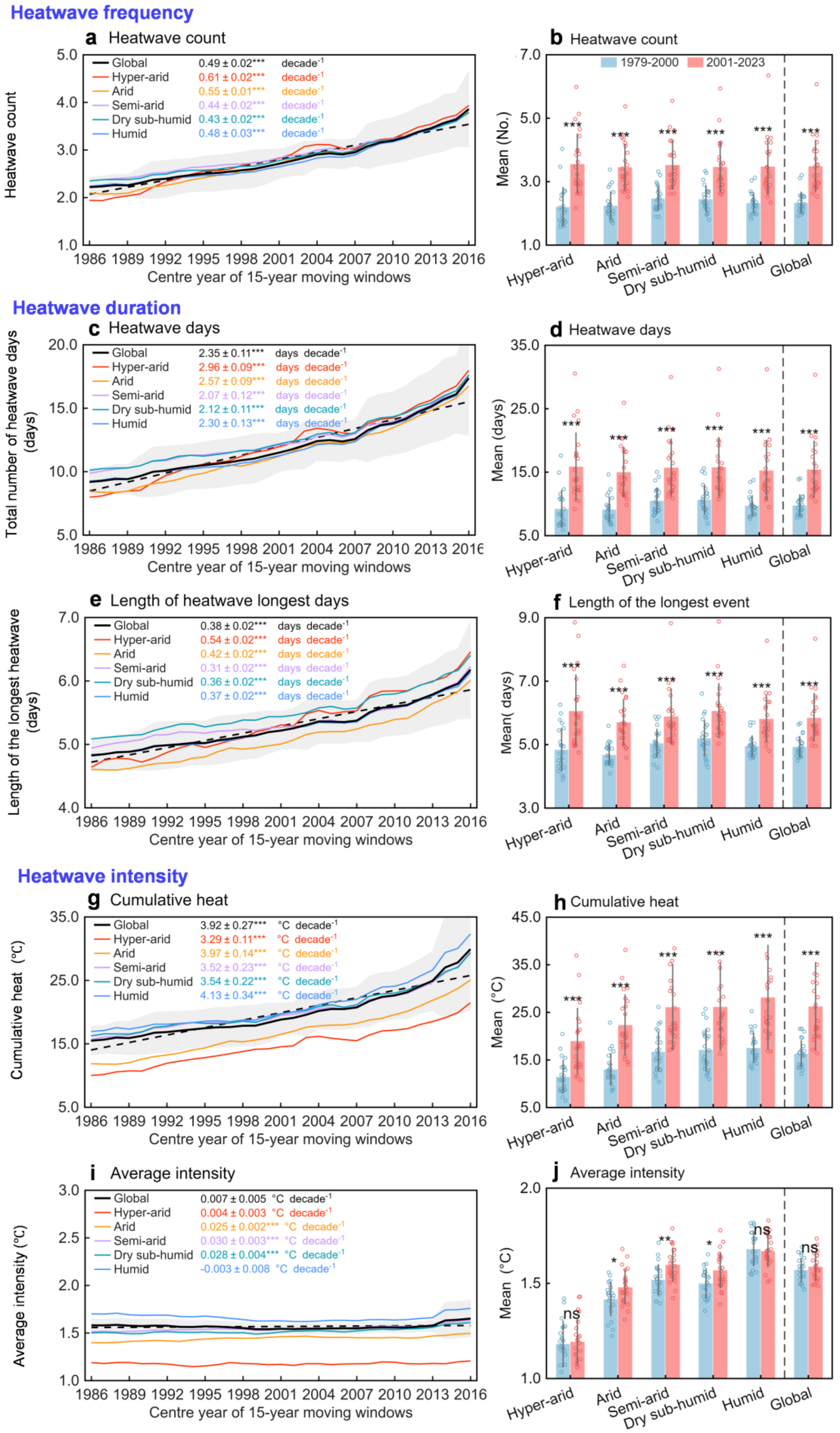

Supplementary Fig. 29 Temporal changes in heatwave frequency, duration, and intensity under the extended heatwave detection window during 1979-2023. The extended window was defined as April-October in the Northern Hemisphere and October-April in the Southern Hemisphere. Panels **a**, **c**, **e**, **g**, and **i** show 15-year centred moving averages of annual area-weighted means for global land and the five aridity zones. In each panel, the black solid line denotes the global moving average, grey shading indicates ±1 SD of the annual area-weighted means within each 15-year window, and the black dashed line shows the fitted linear trend. Colored solid lines represent the moving averages for different aridity zones (i.e., hyper-arid, arid, semi-arid, dry sub-humid, and humid). Numbers in the corresponding colors indicate the linear trend slopes ±1 SE, with asterisks denoting statistical significance (***, $p < 0.001$; **, $p < 0.01$; *, $p < 0.05$). Linear trends were assessed using linear regression based on the 15-year moving-window series (n = 31 moving-window values). Panels **b**, **d**, **f**, **h**, and **j** compare the mean values of each heatwave metric between 1979-2000 (n = 22 years) and 2001-2023 (n = 23 years). Individual points represent annual area-weighted means, and bars and error bars indicate the period mean ±1 SD. Asterisks and "ns" above the bars indicate statistically significant and non-significant differences between the two periods, respectively. Differences between periods were assessed using two-tailed, unpaired Student's *t*-tests. Exact *p*-values for both linear trends and period comparisons are provided in Supplementary Table 3.

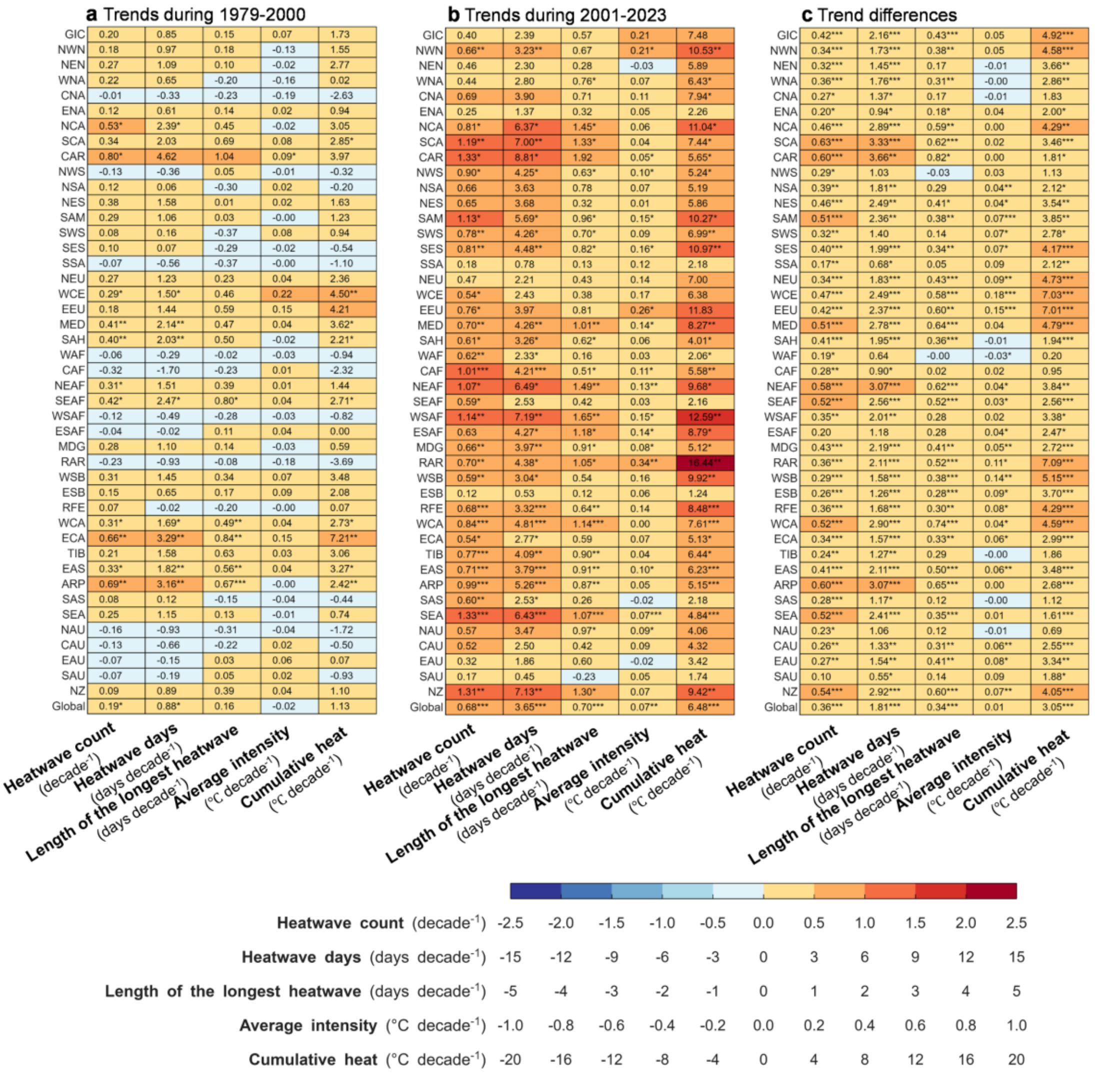

Supplementary Fig. 30 Trends in conventional heatwave metrics during 1979-2000 and 2001-2023, and differences between the two periods globally and across IPCC AR6 reference regions. Heatwaves were detected using the primary heatwave detection window, defined as May-September in the Northern Hemisphere and November-March in the Southern Hemisphere. The panels **a**, **b**, and **c** show decadal trends during 1979-2000 (n = 22 annual values), decadal trends during 2001-2023 (n = 23 annual values), and the differences in trends between the two periods (2001-2023 minus 1979-2000), respectively. Five heatwave metrics are shown: heatwave count, heatwave days, length of the longest heatwave, average intensity, and cumulative heat. Asterisks next to values in the left and middle panels indicate statistically significant trends, whereas those in the right panel indicate statistically significant differences in trends between the two periods (***, $p < 0.001$; **, $p < 0.01$; *, $p < 0.05$). Trend significance was assessed using linear regression, and period differences were assessed using two-sided, unpaired Student's t-tests.

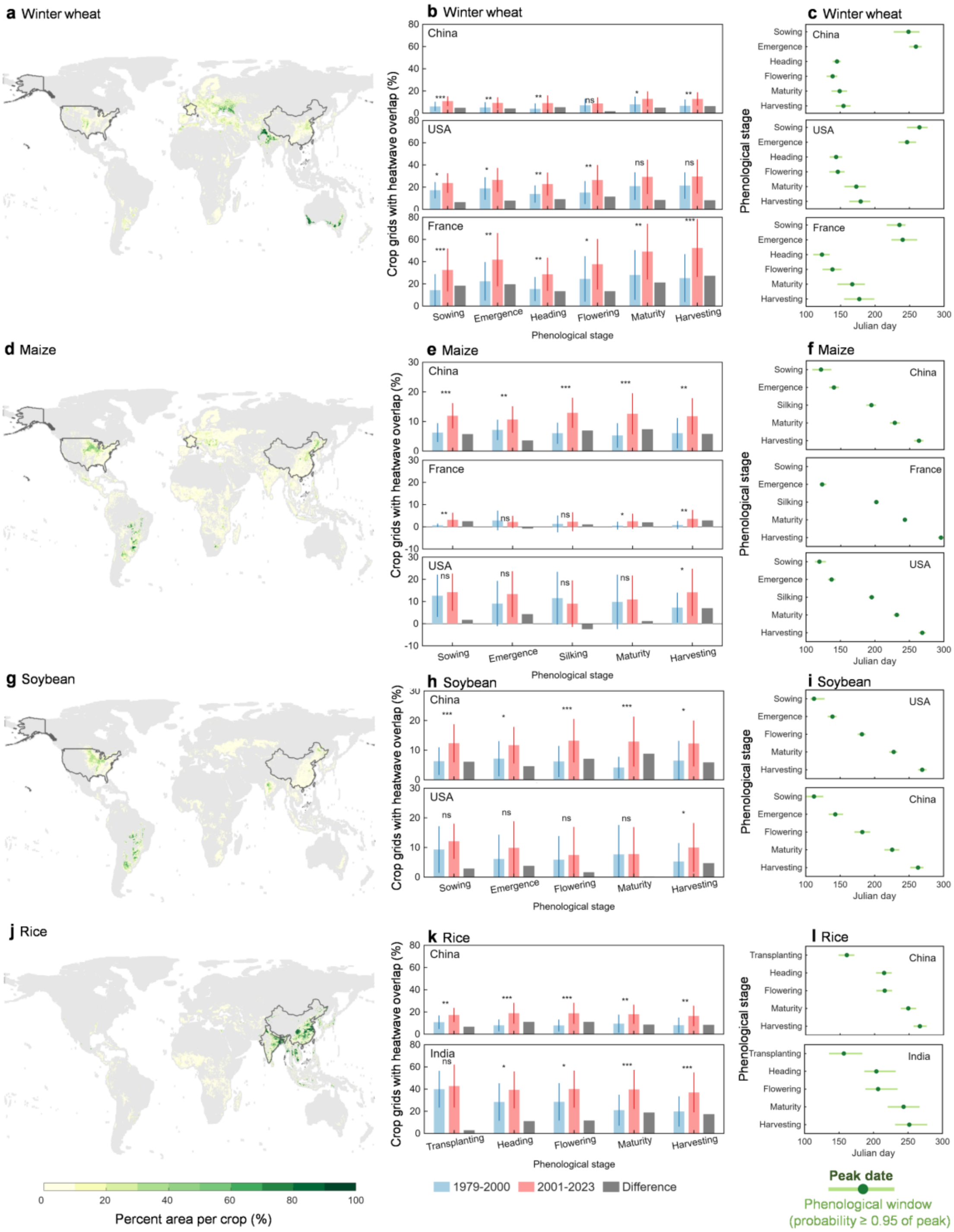

Supplementary Fig. 31 Heatwave-crop phenology overlap across major crops in representative crop-producing countries. The left column shows the spatial distributions of planting areas for (**a**) winter wheat, (**d**) maize, (**g**) soybean, and (**j**) rice using the GEOGLAM crop mask as the background (green shading, percentage of area per grid cell). Heatwave events were identified from ERA5 daily temperature anomalies during 1979-2023 under the extended heatwave detection window, defined as April-October in the Northern Hemisphere and October-April in the Southern Hemisphere. The middle column summarizes the percentage of cultivated crop grid cells that experienced at least one heatwave day during the GCPE-defined phenological window for rainfed crops at each phenological stage in representative crop-producing countries (e.g., China, the United States, France, and India). Blue and red bars represent 1979-2000 and 2001-2023, respectively, while grey bars show the corresponding differences between the two periods (2001-2023 minus 1979-2000). Error bars denote one standard deviation. Asterisks above the bars and "ns" indicate significant (***, $p < 0.001$; **, $p < 0.01$; *, $p < 0.05$) and non-significant differences between the two periods, respectively. The right column shows the phenological calendar windows derived from the GCPE dataset; green dots represent the mean peak date of each phenological stage, and horizontal green lines indicate the corresponding phenological window, defined as the contiguous sequence of days surrounding the peak date for which the daily phenological probability remained at least 95% of its peak value. Basemaps are from Natural Earth (www.naturalearthdata.com). Period differences were assessed using two-sided, unpaired Student's t-tests.

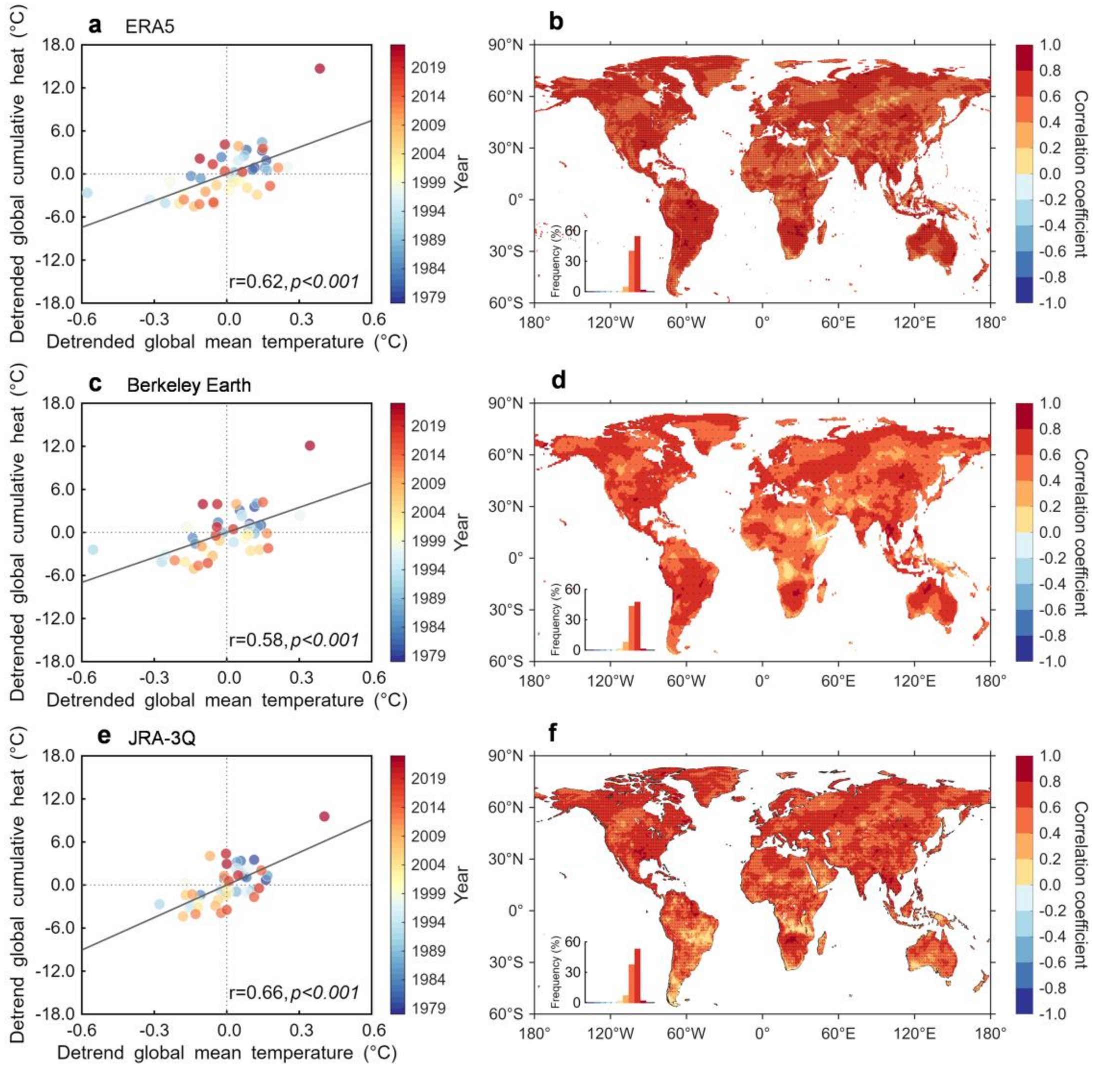

Supplementary Fig. 32 Temporal and spatial correlations between detrended global cumulative heat and detrended mean temperature during 1979-2023 across three datasets. The primary detection window was defined as May-September in the Northern Hemisphere and November-March in the Southern Hemisphere. Both variables were calculated over the corresponding hemispheric warm-season windows. Scatter plots (**a**, **c**, **e**) show the interannual correlations between detrended global cumulative heat and detrended global mean temperature for ERA5, Berkeley Earth, and JRA-3Q, respectively (n = 45 annual values). Maps (**b**, **d**, **f**) show the spatial distributions of grid-cell Pearson correlation coefficients between detrended cumulative heat and detrended mean temperature across grid cells. Basemaps are from Natural Earth (www.naturalearthdata.com).

Supplementary Table 1 Trend estimates for heatwave metrics during 1979-2023 based on 15-year centred moving averages under the primary detection window, globally and across aridity zones. The primary detection window was defined as May-September in the Northern Hemisphere and November-March in the Southern Hemisphere. Metrics include heatwave onset, heatwave ending time, length of heatwave season, heatwave frequency (heatwave count), heatwave duration (heatwave days), and intensity (cumulative heat and average intensity). Linear regression results include slope ± 1 standard error (SE), expressed per decade, the coefficient of determination (R^2), and corresponding *p*-value. Sen's slope analysis reports the slope estimate, Kendall's tau-b, the corresponding *p*-value, and the 95% confidence intervals (CI). All analyses were based on n = 31 moving-window values. Slopes and CI bounds are expressed per decade.

		Linear regression (per decade)			Sen's slope (per decade)				
Variable	**Region**	**Slope ± SE**	**R^2**	**p-value**	**Sen's slope**	**CI lower**	**CI upper**	**Kendall's tau-b**	**p-value**
Heatwave onset (days per decade)	**Global**	**-3.29±0.12**	**0.96**	***p*<0.001**	**-3.25**	**-3.55**	**-2.97**	**-0.96**	***p*<0.001**
	Hyper-arid	-3.56±0.33	0.80	*p*<0.001	-3.39	-4.16	-2.48	-0.79	*p*<0.001
	Arid	-6.02±0.19	0.97	*p*<0.001	-6.03	-6.40	-5.55	-0.93	*p*<0.001
	Semi-arid	-4.16±0.10	0.98	*p*<0.001	-4.16	-4.36	-3.95	-0.96	*p*<0.001
	Dry sub-humid	-3.03±0.17	0.92	*p*<0.001	-3	-3.41	-2.54	-0.9	*p*<0.001
		-2.47±0.16	0.89	*p*<0.001	-2.46	-2.92	-2.08	-0.85	*p*<0.001
Heatwave ending time (days per decade)	**Global**	**5.41±0.12**	**0.98**	***p*<0.001**	**5.4**	**5.12**	**5.66**	**0.97**	***p*<0.001**
	Hyper-arid	8.32±0.62	0.86	*p*<0.001	8.25	7.06	10.07	0.8	*p*<0.001
	Arid	4.04±0.14	0.97	*p*<0.001	4.07	3.76	4.39	0.9	*p*<0.001
	Semi-arid	3.57±0.14	0.96	*p*<0.001	3.51	3.25	3.83	0.92	*p*<0.001
	Dry sub-	4.75±0.20	0.95	*p*<0.001	4.88	4.43	5.37	0.87	*p*<0.001
	humid	5.90± 0.20	0.97	*p*<0.001	6.07	5.6	6.49	0.99	*p*<0.001
Length of heatwave season (days per decade)	**Global**	**8.71±0.17**	**0.99**	***p*<0.001**	**8.56**	**8.19**	**8.97**	**0.99**	***p*<0.001**
	Hyper-arid	11.87±0.42	0.96	*p*<0.001	12.06	11.08	13.28	0.94	*p*<0.001
	Arid	10.06±0.19	0.99	*p*<0.001	10.16	9.82	10.45	0.97	*p*<0.001
	Semi-arid	7.73±0.12	0.99	*p*<0.001	7.7	7.45	8.03	0.99	*p*<0.001
	Dry sub-	7.77±0.14	0.99	*p*<0.001	7.78	7.44	8.1	0.99	*p*<0.001
	humid	8.38±0.26	0.97	*p*<0.001	8.2	7.54	9	0.99	*p*<0.001
Heatwave count (days per decade)	**Global**	**0.32±0.01**	**0.94**	***p*<0.001**	**0.29**	**0.26**	**0.33**	**0.99**	***p*<0.001**
	Hyper-arid	0.38±0.01	0.96	*p*<0.001	0.39	0.35	0.42	0.95	*p*<0.001
	Arid	0.34±0.01	0.95	*p*<0.001	0.32	0.29	0.36	0.97	*p*<0.001
	Semi-arid	0.30±0.01	0.95	*p*<0.001	0.28	0.26	0.31	0.98	*p*<0.001
	Dry sub-	0.30±0.01	0.96	*p*<0.001	0.29	0.27	0.32	0.98	*p*<0.001
	humid	0.31±0.02	0.91	*p*<0.001	0.29	0.24	0.34	0.98	*p*<0.001
Heatwave days (days per decade)	**Global**	**1.52±0.08**	**0.92**	***p*<0.001**	**1.34**	**1.2**	**1.6**	**1**	***p*<0.001**
	Hyper-arid	1.72±0.08	0.95	*p*<0.001	1.73	1.54	1.88	0.94	*p*<0.001
	Arid	1.65±0.08	0.93	*p*<0.001	1.46	1.32	1.7	0.97	*p*<0.001
	Semi-arid	1.42±0.08	0.91	*p*<0.001	1.24	1.12	1.46	0.98	*p*<0.001
	Dry sub-	1.49±0.07	0.94	*p*<0.001	1.4	1.26	1.57	0.97	*p*<0.001
	humid	1.50±0.09	0.91	*p*<0.001	1.36	1.14	1.62	0.99	*p*<0.001
Cumulative heat (°C per decade)	**Global**	**2.43±0.16**	**0.89**	***p*<0.001**	**2.17**	**1.84**	**2.62**	**0.98**	***p*<0.001**
	Hyper-arid	1.57±0.12	0.86	*p*<0.001	1.46	1.23	1.75	0.89	*p*<0.001
	Arid	2.59±0.13	0.93	*p*<0.001	2.32	2.12	2.6	0.96	*p*<0.001
	Semi-arid	2.50±0.16	0.89	*p*<0.001	2.2	1.94	2.58	0.95	*p*<0.001
	Dry sub-	2.63±0.13	0.93	*p*<0.001	2.47	2.26	2.82	0.97	*p*<0.001
	humid	2.53±0.18	0.87	*p*<0.001	2.39	1.91	2.91	0.97	*p*<0.001
Average intensity (°C per decade)	**Global**	**-0.005 ±0.003**	**0.06**	***p*=0.1753**	**-0.008**	**-0.017**	**0.003**	**-0.2**	***p*=0.1261**
	Hyper-arid	-0.022 ±0.004	0.49	*p*<0.001	-0.025	-0.035	-0.014	-0.46	*p*<0.001
	Arid	0.025 ±0.002	0.82	*p*<0.001	0.027	0.022	0.032	0.74	*p*<0.001
	Semi-arid	0.023±0.002	0.83	*p*<0.001	0.021	0.017	0.026	0.82	*p*<0.001
	Dry sub-	0.028 ±0.003	0.74	*p*<0.001	0.027	0.019	0.036	0.75	*p*<0.001
	humid	-0.015 ±0.005	0.28	*p*=0.0023	-0.018	-0.029	-0.005	-0.32	*p*=0.0108

Supplementary Table 2 Area-weighted percentages of global land with positive and negative linear trends and their statistically significant subsets. Metrics include heatwave onset, heatwave ending time, length of heatwave season, heatwave frequency (heatwave count), heatwave duration (heatwave days), and heatwave intensity (cumulative heat and average intensity). Statistical significance was assessed locally and after Benjamini-Hochberg false discovery rate (FDR) correction at $q = 0.05$, following Wilks (2016). “All” denotes the area-weighted percentage of global land showing positive or negative linear trends. “Local sig.” denotes the area-weighted percentage showing locally significant trends ($p < 0.05$), whereas “FDR sig.” denotes the corresponding percentage remaining significant after FDR correction. The primary heatwave detection window covered May-September in the Northern Hemisphere and November-March in the Southern Hemisphere; the extended window covered April-October and October-April, respectively.

Detection window	Variable	Negative trend area (%)			Positive trend area (%)		
		All	Local sig.	FDR sig.	All	Local sig.	FDR sig.
Primary window NH: May-Sep. SH: Nov.-Mar.	Heatwave onset	72.0	13.4	0.4	28.0	1.1	<0.1
	Heatwave ending time	20.4	0.5	0.1	79.6	20.3	4.7
	Length of heatwave season	7.9	0.2	<0.1	92.1	34.4	13.5
	Heatwave count	6.8	0.3	0.1	93.2	43.7	25.8
	Heatwave days	7.2	0.3	0.1	92.8	44.5	26.6
	Cumulative heat	8.4	0.3	0.1	91.6	42.3	22.6
	Average intensity	28.1	1.2	<0.1	71.9	12.4	<0.1
Extended window NH: Apr.-Oct. SH: Oct.-Apr.	Heatwave onset	79.9	21.0	4.9	20.1	0.8	0.1
	Heatwave ending time	16.3	0.4	0.1	83.7	26.9	8.7
	Length of heatwave season	5.4	0.3	0.1	94.6	48.8	33.7
	Heatwave count	4.0	0.3	0.2	96.0	62.0	53.8
	Heatwave days	4.3	0.3	0.2	95.7	62.0	54.1
	Cumulative heat	5.1	0.3	0.2	94.9	61.1	53.1
	Average intensity	21.1	0.9	<0.1	78.9	17.6	0.5

Notes: Wilks, D. S. The stippling shows statistically significant grid points: how research results are routinely overstated and overinterpreted, and what to do about it. *Bull. Am. Meteorol. Soc*. **97**, 2263-2273 (2016).

Supplementary Table 3 Effect estimates and exact *p*-values for Supplementary Figs. 1, 7, 11, 26, 28, and 29. Trends are reported as slope ± 1 SE, and differences as the mean for 2001-2023 minus that for 1979-2000. Statistical tests and sample sizes are defined in the corresponding figure legends.

Figure	Panel	Metric	Group	Analysis	Effect estimate	*p*-value
Supplementary Fig. 1	a	Heatwave onset	Global	Trend in 15-year moving-window means (center years 1986-2016; primary detection window)	-3.29 ± 0.12 days decade^{-1}	2.25×10^{-22}
	a	Heatwave onset	NH		-2.79 ± 0.11 days decade^{-1}	1.63×10^{-21}
	a	Heatwave onset	SH		-4.84 ± 0.32 days decade^{-1}	2.33×10^{-15}
	c	Heatwave ending time	Global		5.41 ± 0.12 days decade^{-1}	6.10×10^{-28}
	c	Heatwave ending time	NH		6.47 ± 0.13 days decade^{-1}	1.34×10^{-29}
	c	Heatwave ending time	SH		1.99 ± 0.29 days decade^{-1}	1.31×10^{-7}
	e	Length of heatwave season	Global		8.71 ± 0.17 days decade^{-1}	3.70×10^{-30}
	e	Length of heatwave season	NH		9.26 ± 0.14 days decade^{-1}	2.03×10^{-33}
	e	Length of heatwave season	SH		6.83 ± 0.51 days decade^{-1}	5.41×10^{-14}
	b	Heatwave onset	Global	1979-2000 vs 2001-2023 (primary detection window)	∆mean= -7.74 days	2.53×10^{-6}
	b	Heatwave onset	NH		∆mean= -6.69 days	4.52×10^{-5}
	b	Heatwave onset	SH		∆mean= -11.40 days	9.03×10^{-4}
	d	Heatwave ending time	Global		∆mean= 11.84 days	5.53×10^{-7}
	d	Heatwave ending time	NH		∆mean= 14.03 days	1.14×10^{-7}
	d	Heatwave ending time	SH		∆mean= 5.28 days	0.1525
	f	Length of heatwave season	Global		∆mean= 19.58 days	3.44×10^{-9}
	f	Length of heatwave season	NH		∆mean= 20.72 days	1.29×10^{-9}
	f	Length of heatwave season	SH		∆mean= 16.68 days	2.02×10^{-4}
Supplementary Fig. 7	a	Heatwave onset	Hyper-arid	1979-2000 vs 2001-2023 (primary detection window)	∆mean= -6.88 days	0.0505
	a	Heatwave onset	Arid		∆mean= -11.85 days	7.48×10^{-6}
	a	Heatwave onset	Semi-arid		∆mean= -10.01 days	5.17×10^{-6}
	a	Heatwave onset	Dry sub-humid		∆mean= -7.27 days	6.29×10^{-4}
	a	Heatwave onset	Humid		∆mean= -6.43 days	3.97×10^{-4}
	a	Heatwave onset	Global		∆mean= -7.74 days	2.53×10^{-6}
	c	Heatwave ending time	Hyper-arid		∆mean= 18.68 days	1.41×10^{-4}
	c	Heatwave ending time	Arid		∆mean= 9.16 days	0.0029
	c	Heatwave ending time	Semi-arid		∆mean= 7.22 days	0.0136
	c	Heatwave ending time	Dry sub-humid		∆mean= 9.95 days	6.46×10^{-4}
	c	Heatwave ending time	Humid		∆mean= 13.02 days	4.92×10^{-7}
	c	Heatwave ending time	Global		∆mean= 11.84 days	5.53×10^{-7}
	e	Length of heatwave season	Hyper-arid		∆mean= 25.56 days	1.69×10^{-6}
	e	Length of heatwave season	Arid		∆mean= 21.01 days	1.28×10^{-8}
	e	Length of heatwave season	Semi-arid		∆mean= 17.23 days	4.03×10^{-8}
	e	Length of heatwave season	Dry sub-humid		∆mean= 17.21 days	1.04×10^{-7}
	e	Length of heatwave season	Humid		∆mean= 19.45 days	3.29×10^{-8}
	e	Length of heatwave season	Global		∆mean= 19.58 days	3.44×10^{-9}
	b	Heatwave onset	Hyper-arid	1979-2000 vs 2001-2023 (extended detection window)	∆mean= -10.97 days	0.0290
	b	Heatwave onset	Arid		∆mean= -20.01 days	1.11×10^{-6}
	b	Heatwave onset	Semi-arid		∆mean= -19.14 days	1.49×10^{-7}
	b	Heatwave onset	Dry sub-humid		∆mean= -15.87 days	4.03×10^{-6}
	b	Heatwave onset	Humid		∆mean= -12.72 days	5.02×10^{-5}
	b	Heatwave onset	Global		∆mean= -14.59 days	7.45×10^{-7}
	d	Heatwave ending time	Hyper-arid		∆mean= 33.29 days	9.92×10^{-7}
	d	Heatwave ending time	Arid		∆mean= 18.49 days	2.81×10^{-5}
	d	Heatwave ending time	Semi-arid		∆mean= 11.61 days	0.0030
	d	Heatwave ending time	Dry sub-humid		∆mean= 14.15 days	4.71×10^{-4}
	d	Heatwave ending time	Humid		∆mean= 19.70 days	1.01×10^{-7}
	d	Heatwave ending time	Global		∆mean= 19.27 days	3.64×10^{-8}
	f	Length of heatwave season	Hyper-arid		∆mean= 44.26 days	6.40×10^{-9}
	f	Length of heatwave season	Arid		∆mean= 38.49 days	1.92×10^{-11}
	f	Length of heatwave season	Semi-arid		∆mean= 30.74 days	1.18×10^{-9}
	f	Length of heatwave season	Dry sub-humid		∆mean= 30.01 days	4.45×10^{-9}
	f	Length of heatwave season	Humid		∆mean= 32.42 days	6.87×10^{-9}
	f	Length of heatwave season	Global		∆mean= 33.86 days	1.09×10^{-10}

Figure	Panel	Metric	Group	Analysis	Effect estimate	*p*-value
Supplementary Fig. 11	a	Heatwave onset	Forest	1979-2023 trend (primary detection window)	-4.04±0.72 days decade^{-1}	1.42×10^{-6}
	a	Heatwave onset	Shurbland		-5.01±0.94 days decade^{-1}	3.40×10^{-6}
	a	Heatwave onset	Grassland		-4.11±0.48 days decade^{-1}	7.43×10^{-11}
	a	Heatwave onset	Cropland		-0.85±0.92 days decade^{-1}	0.3612
	a	Heatwave onset	Barren		-3.68±0.98 days decade^{-1}	4.95×10^{-4}
	a	Heatwave onset	Global noLUC		-3.78±0.45 days decade^{-1}	1.08×10^{-10}
	c	Heatwave ending time	Forest		4.81±1.05 days decade^{-1}	4.09×10^{-5}
	c	Heatwave ending time	Shurbland		3.08±1.25 days decade^{-1}	0.0178
	c	Heatwave ending time	Grassland		4.37±0.76 days decade^{-1}	8.23×10^{-7}
	c	Heatwave ending time	Cropland		6.67±0.98 days decade^{-1}	2.31×10^{-8}
	c	Heatwave ending time	Barren		8.04±1.21 days decade^{-1}	4.49×10^{-8}
	c	Heatwave ending time	Global noLUC		5.07±0.69 days decade^{-1}	4.39×10^{-9}
	e	Length of heatwave season	Forest		8.85±1.20 days decade^{-1}	3.84×10^{-9}
	e	Length of heatwave season	Shurbland		8.09±1.24 days decade^{-1}	6.40×10^{-8}
	e	Length of heatwave season	Grassland		8.48±0.70 days decade^{-1}	1.85×10^{-15}
	e	Length of heatwave season	Cropland		7.52±0.98 days decade^{-1}	1.39×10^{-9}
	e	Length of heatwave season	Barren		11.72±1.11 days decade^{-1}	1.67×10^{-13}
	e	Length of heatwave season	Global noLUC		8.85±0.71 days decade^{-1}	6.97×10^{-16}
	b	Heatwave onset	Forest	1979-2000 vs 2001-2023 (primary detection window)	Δmean= -7.13 days	0.0024
	b	Heatwave onset	Shurbland		Δmean= -11.67 days	5.24×10^{-5}
	b	Heatwave onset	Grassland		Δmean= -8.66 days	1.73×10^{-6}
	b	Heatwave onset	Cropland		Δmean= -1.58 days	0.5151
	b	Heatwave onset	Barren		Δmean= -7.93 days	0.0048
	b	Heatwave onset	Global noLUC		Δmean= -7.88 days	2.99×10^{-6}
	d	Heatwave ending time	Forest		Δmean= 10.89 days	4.97×10^{-4}
	d	Heatwave ending time	Shurbland		Δmean= 8.66 days	0.0098
	d	Heatwave ending time	Grassland		Δmean= 9.94 days	3.35×10^{-5}
	d	Heatwave ending time	Cropland		Δmean= 15.80 days	9.30×10^{-7}
	d	Heatwave ending time	Barren		Δmean= 16.61 days	5.24×10^{-5}
	d	Heatwave ending time	Global noLUC		Δmean= 11.42 days	1.65×10^{-6}
	f	Length of heatwave season	Forest		Δmean= 18.02 days	2.42×10^{-5}
	f	Length of heatwave season	Shurbland		Δmean= 20.33 days	2.48×10^{-7}
	f	Length of heatwave season	Grassland		Δmean= 18.60 days	5.27×10^{-9}
	f	Length of heatwave season	Cropland		Δmean= 17.37 days	3.45×10^{-7}
	f	Length of heatwave season	Barren		Δmean= 24.53 days	2.21×10^{-7}
	f	Length of heatwave season	Global noLUC		Δmean= 19.30 days	5.13×10^{-9}
Supplementary Fig. 26	b	Heatwave count	Hyper-arid	1979-2000 vs 2001-2023 (primary detection window)	Δmean= 0.86 events	3.50×10^{-5}
	b	Heatwave count	Arid		Δmean= 0.75 events	2.66×10^{-6}
	b	Heatwave count	Semi-arid		Δmean= 0.72 events	2.37×10^{-6}
	b	Heatwave count	Dry sub-humid		Δmean= 0.70 events	9.63×10^{-6}
	b	Heatwave count	Humid		Δmean= 0.74 events	2.70×10^{-6}
	b	Heatwave count	Global		Δmean= 0.74 events	1.37×10^{-6}
	d	Heatwave days	Hyper-arid		Δmean= 3.97 days	2.20×10^{-4}
	d	Heatwave days	Arid		Δmean= 3.84 days	5.85×10^{-6}
	d	Heatwave days	Semi-arid		Δmean= 3.63 days	5.06×10^{-5}
	d	Heatwave days	Dry sub-humid		Δmean= 3.66 days	7.48×10^{-5}
	d	Heatwave days	Humid		Δmean= 3.65 days	9.31×10^{-6}
	d	Heatwave days	Global		Δmean= 3.68 days	8.15×10^{-6}
	f	Length of the longest heatwave	Hyper-arid		Δmean= 0.70 days	0.0090
	f	Length of the longest heatwave	Arid		Δmean= 0.80 days	8.13×10^{-6}
	f	Length of the longest heatwave	Semi-arid		Δmean= 0.64 days	0.0020
	f	Length of the longest heatwave	Dry sub-humid		Δmean= 0.70 days	0.0015
	f	Length of the longest heatwave	Humid		Δmean= 0.66 days	5.19×10^{-5}
	f	Length of the longest heatwave	Global		Δmean= 0.68 days	5.43×10^{-5}
	h	Cumulative heat	Hyper-arid		Δmean= 3.78 ℃	0.0054
	h	Cumulative heat	Arid		Δmean= 6.04 ℃	5.81×10^{-6}
	h	Cumulative heat	Semi-arid		Δmean= 6.70 ℃	1.45×10^{-4}
	h	Cumulative heat	Dry sub-humid		Δmean= 6.78 ℃	1.80×10^{-4}
	h	Cumulative heat	Humid		Δmean= 6.38 ℃	2.41×10^{-5}
	h	Cumulative heat	Global		Δmean= 6.11 ℃	1.97×10^{-5}

Figure	Panel	Metric	Group	Analysis	Effect estimate	*p*-value
Supplementary Fig. 26	j	Average intensity	Hyper-arid	1979-2000 vs 2001-2023 (primary detection window)	Δmean= -0.04 °C	0.3697
	j	Average intensity	Arid		Δmean= 0.06 °C	0.0311
	j	Average intensity	Semi-arid		Δmean= 0.07 °C	0.0112
	j	Average intensity	Dry sub-humid		Δmean= 0.08 °C	0.0118
	j	Average intensity	Humid		Δmean= -0.01 °C	0.6458
	j	Average intensity	Global		Δmean= 0.01 °C	0.8252
Supplementary Fig. 28	a	Heatwave count	Global	Trend in 15-year centred moving-window means (1986-2016; primary detection window)	0.32 ± 0.01 events decade^{-1}	2.74×10^{-19}
	a	Heatwave count	North		0.33 ± 0.01 events decade^{-1}	9.07×10^{-22}
	a	Heatwave count	South		0.26 ± 0.03 events decade^{-1}	7.91×10^{-11}
	c	Heatwave days	Global		1.52 ± 0.08 days decade^{-1}	8.81×10^{-18}
	c	Heatwave days	North		1.62 ± 0.07 days decade^{-1}	1.99×10^{-20}
	c	Heatwave days	South		1.19 ± 0.14 days decade^{-1}	1.87×10^{-9}
	e	Length of the longest heatwave	Global		0.27 ± 0.02 days decade^{-1}	1.17×10^{-16}
	e	Length of the longest heatwave	North		0.30 ± 0.01 days decade^{-1}	9.18×10^{-20}
	e	Length of the longest heatwave	South		0.18 ± 0.03 days decade^{-1}	8.09×10^{-7}
	g	Cumulative heat	Global		2.43 ± 0.16 °C decade^{-1}	1.83×10^{-15}
	g	Cumulative heat	North		2.68 ± 0.15 °C decade^{-1}	2.12×10^{-17}
	g	Cumulative heat	South		1.61 ± 0.24 °C decade^{-1}	1.96×10^{-7}
	i	Average intensity	Global		−0.005 ± 0.003 decade^{-1}	0.1753
	i	Average intensity	North		−0.007 ± 0.004 °C decade^{-1}	0.0908
	i	Average intensity	South		−0.0001 ± 0.0051 °C decade^{-1}	0.9855
	b	Heatwave count	Global	1979-2000 vs 2001-2023 (primary detection window)	Δmean = 0.74 events	1.37×10^{-6}
	b	Heatwave count	North		Δmean = 0.77 events	2.57×10^{-7}
	b	Heatwave count	South		Δmean = 0.68 events	0.0014
	d	Heatwave days	Global		Δmean = 3.68 days	8.15×10^{-6}
	d	Heatwave days	North		Δmean = 3.86 days	1.47×10^{-6}
	d	Heatwave days	South		Δmean = 3.24 days	0.0044
	f	Length of the longest heatwave	Global		Δmean = 0.68 days	5.46×10^{-5}
	f	Length of the longest heatwave	North		Δmean = 0.75 days	1.72×10^{-5}
	f	Length of the longest heatwave	South		Δmean = 0.51 days	0.0265
	h	Cumulative heat	Global		Δmean = 6.11 °C	1.97×10^{-5}
	h	Cumulative heat	North		Δmean = 6.70 °C	6.64×10^{-6}
	h	Cumulative heat	South		Δmean = 4.54 °C	0.0088
	j	Average intensity	Global		Δmean = 0.01 °C	0.8131
	j	Average intensity	North		Δmean = 0.01 °C	0.7890
	j	Average intensity	South		Δmean = 0.01 °C	0.7084
Supplementary Fig. 29	a	Heatwave count	Hyper-arid	Trend in 15-year centred moving-window means (1986-2016; extended detection window)	0.49±0.02 events decade^{-1}	2.08×10^{-20}
	a	Heatwave count	Arid		0.61±0.02 events decade^{-1}	5.37×10^{-26}
	a	Heatwave count	Semi-arid		0.55±0.01 events decade^{-1}	4.16×10^{-27}
	a	Heatwave count	Dry sub-humid		0.44±0.02 events decade^{-1}	6.04×10^{-21}
	a	Heatwave count	Humid		0.43±0.02 events decade^{-1}	5.14×10^{-20}
	a	Heatwave count	Global		0.48±0.03 events decade^{-1}	1.87×10^{-17}
	c	Heatwave days	Hyper-arid		2.35±0.11 days decade^{-1}	7.39×10^{-19}
	c	Heatwave days	Arid		2.96±0.09 days decade^{-1}	4.21×10^{-25}
	c	Heatwave days	Semi-arid		2.57±0.09 days decade^{-1}	2.41×10^{-23}
	c	Heatwave days	Dry sub-humid		2.07±0.12 days decade^{-1}	3.04×10^{-17}
	c	Heatwave days	Humid		2.12±0.11 days decade^{-1}	4.17×10^{-18}
	c	Heatwave days	Global		2.30±0.13 days decade^{-1}	5.47×10^{-17}
	e	Length of the longest heatwave	Hyper-arid		0.38±0.02 days decade^{-1}	8.26×10^{-19}
	e	Length of the longest heatwave	Arid		0.54±0.02 days decade^{-1}	5.37×10^{-23}
	e	Length of the longest heatwave	Semi-arid		0.42±0.02 days decade^{-1}	3.01×10^{-20}
	e	Length of the longest heatwave	Dry sub-humid		0.31±0.02 days decade^{-1}	9.47×10^{-14}
	e	Length of the longest heatwave	Humid		0.36±0.02 days decade^{-1}	5.50×10^{-17}
	e	Length of the longest heatwave	Global		0.37±0.02 days decade^{-1}	1.48×10^{-18}

Figure	Panel	Metric	Group	Analysis	Effect estimate	*p*-value
Supplementary Fig. 29	g	Cumulative heat	Hyper-arid	Trend in 15-year centred moving-window means (1986-2016; extended detection window)	3.92±0.27 °C days decade^{-1}	5.28×10^{-15}
	g	Cumulative heat	Arid		3.29±0.11 °C days decade^{-1}	8.22×10^{-24}
	g	Cumulative heat	Semi-arid		3.97±0.14 °C days decade^{-1}	1.38×10^{-22}
	g	Cumulative heat	Dry sub-humid		3.52±0.23 °C days decade^{-1}	2.20×10^{-15}
	g	Cumulative heat	Humid		3.54±0.22 °C days decade^{-1}	4.91×10^{-16}
	g	Cumulative heat	Global		4.13±0.34 °C days decade^{-1}	4.79×10^{-13}
	i	Average intensity	Hyper-arid		0.007±0.005 °C decade^{-1}	0.2060
	i	Average intensity	Arid		0.004±0.003 °C decade^{-1}	0.1540
	i	Average intensity	Semi-arid		0.025±0.002 °C decade^{-1}	1.85×10^{-11}
	i	Average intensity	Dry sub-humid		0.030±0.003 °C decade^{-1}	4.88×10^{-12}
	i	Average intensity	Humid		0.028±0.004 °C decade^{-1}	2.11×10^{-8}
	i	Average intensity	Global		−0.003±0.008 °C decade^{-1}	0.0079
Supplementary Fig. 29	b	Heatwave count	Hyper-arid	1979-2000 vs 2001-2023 (extended detection window)	Δmean = 1.35 events	1.28×10^{-6}
	b	Heatwave count	Arid		Δmean = 1.21 events	4.55×10^{-8}
	b	Heatwave count	Semi-arid		Δmean = 1.05 events	7.66×10^{-7}
	b	Heatwave count	Dry sub-humid		Δmean = 1.01 events	4.48×10^{-6}
	b	Heatwave count	Humid		Δmean = 1.14 events	1.23×10^{-6}
	b	Heatwave count	Global		Δmean = 1.15 events	3.10×10^{-7}
	d	Heatwave days	Hyper-arid		Δmean = 6.68 days	6.13×10^{-6}
	d	Heatwave days	Arid		Δmean = 5.92 days	1.71×10^{-7}
	d	Heatwave days	Semi-arid		Δmean = 5.25 days	1.41×10^{-5}
	d	Heatwave days	Dry sub-humid		Δmean = 5.12 days	4.27×10^{-5}
	d	Heatwave days	Humid		Δmean = 5.56 days	5.05×10^{-6}
	d	Heatwave days	Global		Δmean = 5.63 days	2.16×10^{-6}
	f	Length of the longest heatwave	Hyper-arid		Δmean = 1.23 days	8.41×10^{-5}
	f	Length of the longest heatwave	Arid		Δmean = 1.03 days	3.50×10^{-7}
	f	Length of the longest heatwave	Semi-arid		Δmean = 0.85 days	2.13×10^{-4}
	f	Length of the longest heatwave	Dry sub-humid		Δmean = 0.87 days	2.93×10^{-4}
	f	Length of the longest heatwave	Humid		Δmean = 0.86 days	1.26×10^{-5}
	f	Length of the longest heatwave	Global		Δmean = 0.92 days	6.51×10^{-6}
	h	Cumulative heat	Hyper-arid		Δmean = 7.53 °C	4.42×10^{-5}
	h	Cumulative heat	Arid		Δmean = 9.28 °C	3.46×10^{-7}
	h	Cumulative heat	Semi-arid		Δmean = 9.35 °C	7.18×10^{-5}
	h	Cumulative heat	Dry sub-humid		Δmean = 9.08 °C	1.60×10^{-4}
	h	Cumulative heat	Humid		Δmean = 10.64 °C	7.73×10^{-5}
	h	Cumulative heat	Global		Δmean = 9.94 °C	1.94×10^{-5}
	j	Average intensity	Hyper-arid		Δmean = 0.01 °C	0.7263
	j	Average intensity	Arid		Δmean = 0.06 °C	0.0254
	j	Average intensity	Semi-arid		Δmean = 0.08 °C	0.0039
	j	Average intensity	Dry sub-humid		Δmean = 0.07 °C	0.0110
	j	Average intensity	Humid		Δmean = -0.01 °C	0.6898
	j	Average intensity	Global		Δmean = 0.02 °C	0.4147

Supplementary References

64. Masson-Delmotte, V., *et al.* Climate change 2021: the physical science basis. *Contribution of working group I to the sixth assessment report of the intergovernmental panel on climate change* **2**, 2391 (2021).
65. Wang, Y., Hessen, D.O., Samset, B.H. & Stordal, F. Evaluating global and regional land warming trends in the past decades with both MODIS and ERA5-Land land surface temperature data. *Remote Sens. Environ*. **280**, 113197 (2022).
66. Lhotka, O. & Kyselý, J. Three-dimensional analysis reveals diverse heat wave types in Europe. *Commun. Earth Environ.* **5**, 323 (2024).
67. Kim, J.H., Nam, S.H., Kim, M.K., Serrano-Notivoli, R. & Tejedor, E. The 2022 record-high heat waves over southwestern Europe and their underlying mechanism. *Weather Clim. Extremes* **46**, 100729 (2024).
68. Zhang, X. *et al.* Increased impact of heat domes on 2021-like heat extremes in North America under global warming. *Nat. Commun.* **14**, 1690 (2023).
69. Davini, P. & D'Andrea, F. From CMIP3 to CMIP6: Northern Hemisphere atmospheric blocking simulation in present and future climate. *J. Clim*. **33**, 10021-10038 (2020).
70. Miralles, D. G., Gentine, P., Seneviratne, S. I. & Teuling, A. J. Land-atmospheric feedbacks during droughts and heatwaves: state of the science and current challenges. *Ann. N. Y. Acad. Sci.* **1436**, 19-35 (2019).